# Explainable ensemble learning reveals site-driven $d_z^2$ orbital-occupancy tuning for enhanced hydrogen evolution on metal-doped Ni-loaded BN catalysts

Hang Zhang[a,b,1], Zishan Luo [a,b,1], Xi Sun[a,b,1], Wenhao Yan[a,b], Jiawei Li[a,b], Xiangxi Fan[a,b], Yihang Hu[a,b], Tao Zhang[a,b], Hong Cui[a,b,*], Weizhi Tian[a,b,**], Rong Feng[a,b], Guanqi Wang[a,b], Ganglin Cao[a,b], Jie Tian[a,b], Hongkuan Yuan[c]

[a] School of Mechanical Engineering, Shaanxi University of Technology, Hanzhong, Shaanxi, 723001, China

[b] Shaanxi Key Laboratory of Industrial Automation, Shaanxi University of Technology, Hanzhong, Shaanxi, 723001, China

[c] School of Physical Science and Technology, Southwest University, Chongqing, 400715, China

[1]These authors contributed equally to this work.

*Corresponding author 1: hongcui@snut.edu.cn (Hong Cui)

** Corresponding author 2: tianweizhi@snut.edu.cn (Weizhi Tian)

Supplementary Materials:

Supplementary Note 2

Supplementary Tables 1-7

Supplementary Figures 1-25

**Supplementary Note 1**

**DFT calculations**

All calculations in this study were carried out using spin-polarized density functional theory (DFT) as implemented in the Vienna Ab-initio Simulation Package (VASP)[1]. The electronic exchange-correlation interactions were treated using the Perdew-Burke-Ernzerhof (PBE) functional within the generalized gradient approximation (GGA) [2, 3]. The Brillouin zone is sampled using a 3 × 3 × 1 Monkhorst−Pack K-point grid, with the truncation energy of the plane-wave basis group set to 520 eV. The correction for van der Waals interactions was implemented using Grimme's DFT-D3 method. The net

charge transfer between the substrate and intermediates was assessed by Bader charge analysis. The ICOHP analysis was performed by LOBSTER. Ab initio molecular dynamics (AIMD) simulations were performed to investigate the thermal stability of the Ni-$TM_2$@BN structure (a = 10 Å, b = 13 Å) at 300 K, the total simulation time was 3 ps with a time step of 1 fs.

**Formation energy and dissolution potential of DACs**

The formation energy refers to the difficulty of synthesizing a catalyst from substrate, namely thermodynamical stability. The dissolution potential represents electrochemical stability, meaning whether the metal active center will fall off the structure and dissolve into the electrolyte. The formation energy and dissolution energy of DACs are defined as:

$$E_{\mathrm{f1}} = E_{\mathrm{Ni@BN}} + \mu_{\mathrm{B}} - (E_{\mathrm{BN}} + \mu_{\mathrm{Ni}})$$

$$E_{\mathrm{f}} = E_{\mathrm{Ni\text{-}TM2@BN}} + \mu_{\mathrm{B}} - (E_{\mathrm{Ni@BN}} + \mu_{\mathrm{TM2}})$$

$$\mathrm{U_{diss}} = \mathrm{U^0_{diss}(metal, bulk)} - \frac{\mathrm{E_f}}{ne}$$

where $E_{\mathrm{Ni@BN}}$, $E_{\mathrm{Ni\text{-}TM2@BN}}$ and $E_{\mathrm{BN}}$ represent the energies of the single-metal Ni-doped BN structure, the bimetal-doped BN structure, and the pristine BN structure, respectively. $\mu_{\mathrm{Ni}}$, $\mu_{\mathrm{B}}$, $\mu_{\mathrm{TM2}}$,correspond to the energies of the Ni atom, the coordinated environment B, the doped metal TM2, respectively. $U^{0}_{diss}(metal,bulk)$ and $n$ are the standard dissolution potential of bulk metal and the number of electrons involved in the dissolution, respectively.

**Adsorption energy**

The adsorption energy calculation of Ni-TM2@BN structures was performed as follows.

$$\Delta E_{*\mathrm{H}} = E_{\mathrm{slab*H}} - E_{\mathrm{slab}} - E_{\mathrm{H}}$$

Here, $E_{\mathrm{slab*H}}$, $E_{\mathrm{slab}}$ and $E_{\mathrm{X}}$ respectively represent the Ni-TM2@BN adsorption

intermediate X, the Ni-TM2@BN substrate, and the intermediate energy.

**HER mechanism**

HER in acidic conditions with free energy equations:

$$* + H^+ + e^- \rightarrow H* \rightarrow * + 0.5H_2$$

$$\Delta G_{H*} = (E_{H*} - E_* - 0.5E_{H_2}) - (ZPE_{H*} - ZPE_* - 0.5ZPE_{H_2}) - T(S_{H*} - S_* - 0.5S_{H_2})$$

HER in basic conditions is the same as below with the samefree energy equation as eqn :

$$* + H_2O + e^- \rightarrow H* \rightarrow * + OH \rightarrow * + 0.5H_2$$

**Supplementary Note 2**

**Base Learner Construction**

The machine learning models are implemented in a Python 3 environment using Scikit-Learn[4]. The Adsorption Energy model is built using Extreme Gradient Boosting (XGB)[5], Random Forest Regression (RFR) [6], Support Vector Regression (GBR) [7]. These algorithms are highly iterative and handle data with nonlinear relationships. By predicting feature–target relationships, SISSO helps analyze ML models. The results of the regression algorithms are evaluated using two statistical regression metrics: Root Mean Square Error (*RMSE*) and Coefficient of Determination ($R^2$), with calculation methods provided in Eq. S2-S3. The data is split into 80% training set and 20% testing set for model training.

**SISSO algorithm**

The operation process of the SISSO algorithm is mainly divided into two stages: feature screening and sparsification model construction[8].

Sure Independence Screening (SIS): First, a set of potential descriptors is generated from a large pool of features, which are usually generated by a series of mathematical operations (e.g., addition, multiplication, logarithm, etc.) from atomic properties, geometrical parameters, etc. The SIS step filters out the most relevant

features from these features with respect to the target variables (e.g., material properties) through correlation analysis, which reduces the spatial dimensions of the features. Reducing the feature space dimension.

Sparsifying Operator (SO): Among the filtered features, SO further extracts a small number of the most representative descriptors, usually using the L0 paradigm to construct a sparse model. This step is optimized to ensure that the retained features have the maximum impact on the target variables while maintaining the simplicity of the model.

Ultimately, the five after feature engineering are used as the eigenvalues, and the adsorption energy is used as the target values as inputs into the SISSO model, outputting a linear model with a high degree of interpretability.

**Table S1** Model parameters of the SISSO algorithm.

| | Parameters |
|---|---|
| SISSO | ptype=1，ntask=1<br>task_weighting=1，scmt=.false.<br>desc_dim=1，nsample= 999<br>! nsample = (n1, n2, ...) ，restart=0<br>nsf= 4，ops='(+)(-)(*)(/)(^-1)(^2) (^3) '<br>fcomplexity=3，funit=(1:7)<br>fmax_min=1e-3，fmax_max=1e-5<br>nf_sis=400，method_so= 'L0'<br>nl1l0= 1，fit_intercept=.true.<br>metric= 'RMSE'，nmodels=100<br>! isconvex=(1,1,...)，bwidth=0.001 |

**Table S2** Optimal Hyperparameters Selected for the Three Ensemble learning$\triangle G_{H1*}$.

| Model | AdaBoost-RFR | AdaBoost-GBR | AdaBoost-XGB |
|---|---|---|---|
| Optimal Hyperparameter | learning_rate': 0.14, 'loss': 'linear', 'n_estimators': 40 cv=4 | 'learning_rate':0.04, 'n_estimators': 40, 'random_state': 0 cv=4 | 'learning_rate': 0.18, 'n_estimators': 60 cv=4 |

**Table S3** Optimal Hyperparameters Selected for the Three Ensemble learning($\triangle G_{H2*}$).

| Model | AdaBoost-RFR | AdaBoost-GBR | AdaBoost-XGB |
|---|---|---|---|
| Optimal Hyperparameter | 'learning_rate':1.0, 'n_estimators':20, cv=4 | 'learning_rate':0.8, 'loss': 'linear' 'n_estimators':50, cv=4 | 'learning_rate':0.18, 'n_estimators':40, cv=4 |

**Table S4 Formation energy ($E_f$) of Ni-TM2@BN at different sites**

| $E_f$ | OC1 | OC2 | OC3 | OC4 | OC5 | OC6 | OC7 | OC8 |
|---|---|---|---|---|---|---|---|---|
| Ni-Sc | -4.79 | -4.86 | -4.00 | -4.03 | 1.64 | -4.08 | -3.81 | -4.03 |
| Ni-Ti | -6.14 | -6.22 | -5.06 | -4.99 | -5.09 | -4.88 | -4.66 | -4.99 |
| Ni-V | -4.63 | -4.70 | -3.20 | -3.28 | -3.36 | -3.16 | -3.07 | -3.28 |
| Ni-Cr | -2.44 | -2.60 | -1.33 | -1.40 | -1.55 | -1.44 | -1.42 | -1.40 |
| Ni-Mn | -2.08 | -2.20 | -0.88 | -0.92 | -0.92 | -0.83 | -0.58 | -0.92 |
| Ni-Fe | -2.75 | -2.76 | -1.02 | -1.08 | -1.12 | -1.05 | -1.03 | -1.08 |
| Ni-Co | -2.30 | -2.38 | -1.05 | -0.98 | 0.66 | -1.22 | -1.18 | -0.98 |
| Ni-Ni | -1.84 | -1.95 | -0.42 | -0.49 | -0.56 | -0.52 | -0.29 | -0.49 |
| Ni-Y | -4.72 | -4.69 | -3.80 | -3.80 | -4.11 | -3.85 | -3.54 | -3.80 |
| Ni-Zr | -7.00 | -6.91 | -5.87 | -5.58 | -5.84 | -5.47 | -5.22 | -5.58 |
| Ni-Nb | -5.76 | -6.04 | -4.46 | -4.21 | -4.42 | -4.05 | -3.76 | -4.21 |
| Ni-Mo | -4.85 | -5.34 | -3.54 | -3.30 | -3.48 | -3.31 | -3.06 | -3.30 |
| Ni-Tc | -2.44 | -2.88 | -2.99 | -1.09 | -1.19 | -1.02 | -0.76 | -1.09 |
| Ni-Ru | -3.44 | -3.87 | -2.01 | -2.07 | -2.15 | -2.09 | -1.84 | -2.07 |
| Ni-Rh | -2.46 | -2.79 | -1.31 | -1.47 | -1.54 | -1.49 | -1.21 | -1.47 |
| Ni-Pd | 0.52 | 0.29 | 1.88 | 1.76 | 1.70 | 1.78 | 2.13 | 1.76 |
| Ni-Hf | -7.15 | -7.06 | -8.87 | -5.83 | -6.07 | -5.77 | -5.71 | -5.83 |
| Ni-Ta | -7.54 | -7.26 | -5.85 | -5.63 | -5.78 | -5.47 | -5.34 | -5.63 |
| Ni-W | -5.37 | -5.77 | -3.63 | -3.33 | -3.46 | -3.24 | -3.16 | -3.33 |
| Ni-Re | -3.80 | -4.15 | -2.07 | -2.12 | -2.21 | -1.76 | -1.87 | -2.12 |
| Ni-Os | -4.33 | -4.22 | -2.07 | -1.93 | -2.03 | -1.92 | -1.87 | -1.93 |
| Ni-Ir | -3.42 | -3.63 | -1.78 | -1.85 | -1.95 | -1.88 | -1.85 | -1.85 |
| Ni-Pt | -1.51 | -1.48 | 0.21 | 0.34 | 0.30 | 0.34 | 0.47 | 0.34 |

**Table S5 Dissolution potential ($U_{diss}$) of Ni-TM2@BN at different sites**

| $U_{diss}$ | *n* | $U_{diss}^{0}$ | OC1 | OC2 | OC3 | OC4 | OC5 | OC6 | OC7 | OC8 |
|---|---|---|---|---|---|---|---|---|---|---|
| Ni-Sc | 3 | -2.08 | -0.48 | -0.46 | -0.75 | -0.74 | -2.63 | -0.72 | -0.81 | -0.71 |
| Ni-Ti | 3 | -1.63 | 1.44 | 1.48 | 0.90 | 0.86 | 0.92 | 0.81 | 0.70 | 0.76 |
| Ni-V | 2 | -1.18 | 1.14 | 1.17 | 0.42 | 0.46 | 0.50 | 0.40 | 0.35 | 0.45 |
| Ni-Cr | 2 | -0.91 | 0.31 | 0.39 | -0.24 | -0.21 | -0.14 | -0.19 | -0.20 | -0.19 |
| Ni-Mn | 2 | -1.19 | -0.15 | -0.09 | -0.75 | -0.73 | -0.73 | -0.78 | -0.90 | -0.78 |
| Ni-Fe | 2 | -0.45 | 0.93 | 0.93 | 0.06 | 0.09 | 0.11 | 0.07 | 0.07 | 1.57 |
| Ni-Co | 2 | -0.28 | 0.87 | 0.91 | 0.25 | 0.21 | -0.61 | 0.33 | 0.31 | 0.33 |
| Ni-Ni | 2 | -0.26 | 0.66 | 0.72 | -0.05 | -0.01 | 0.02 | 0.00 | -0.12 | -0.03 |
| Ni-Y | 3 | -2.37 | -0.80 | -0.81 | -1.10 | -1.10 | -1.00 | -1.09 | -1.19 | -1.07 |
| Ni-Zr | 4 | -1.45 | 0.30 | 0.28 | 0.02 | -0.06 | 0.01 | -0.08 | -0.15 | -0.02 |
| Ni-Nb | 3 | -1.1 | 0.82 | 0.91 | 0.39 | 0.30 | 0.37 | 0.25 | 0.15 | 0.32 |
| Ni-Mo | 3 | -0.2 | 1.42 | 1.58 | 0.98 | 0.90 | 0.96 | 0.90 | 0.82 | 0.92 |
| Ni-Ru | 2 | 0.46 | 2.18 | 2.40 | 1.47 | 1.50 | 1.54 | 1.50 | 1.38 | 1.50 |
| Ni-Rh | 2 | 0.6 | 1.83 | 1.99 | 1.25 | 1.33 | 1.37 | 1.34 | 1.21 | 1.34 |
| Ni-Pd | 2 | 0.95 | 0.69 | 0.80 | 0.01 | 0.07 | 0.10 | 0.06 | -0.11 | 0.03 |
| Ni-Hf | 4 | -1.55 | 0.24 | 0.22 | 0.67 | -0.09 | -0.03 | -0.11 | -0.12 | -0.06 |
| Ni-Ta | 3 | -0.6 | 1.91 | 1.82 | 1.35 | 1.28 | 1.33 | 1.22 | 1.18 | 1.27 |
| Ni-W | 3 | 0.1 | 1.89 | 2.02 | 1.31 | 1.21 | 1.25 | 1.18 | 1.15 | 1.21 |
| Ni-Re | 3 | 0.3 | 1.57 | 1.68 | 0.99 | 1.01 | 1.04 | 0.89 | 0.92 | 0.99 |
| Ni-Os | 8 | 0.84 | 1.38 | 1.37 | 1.10 | 1.08 | 1.09 | 1.08 | 1.07 | 1.08 |
| Ni-Ir | 3 | 1.16 | 2.30 | 2.37 | 1.75 | 1.78 | 1.81 | 1.79 | 1.78 | 1.79 |
| Ni-Pt | 2 | 1.18 | 1.93 | 1.92 | 1.08 | 1.01 | 1.03 | 1.01 | 0.94 | 0.98 |

**Table S6** DFT-calculated hydrogen adsorption free energies and corresponding doping distances of Ni–TM2@BN structures with favorable HER performance at different doping sites.

| H-Ni | $d_{Ni-TM2}$ | $\triangle G_{H1*}$ | H-Ni | $d_{Ni-TM2}$ | $\triangle G_{H1*}$ |
|---|---|---|---|---|---|
| Ni-Sc(OC1) | 2.52 | 0.19 | Ni-Nb(OC7) | 6.65 | 0.12 |
| Ni-V(OC2) | 2.57 | -0.21 | Ni-Tc(OC7) | 6.65 | 0.19 |
| Ni-Fe(OC2) | 2.57 | -0.21 | Ni-Ti(OC8) | 8.69 | -0.04 |
| Ni-Pd(OC6) | 5.03 | -0.19 | Ni-Zr(OC8) | 8.69 | 0.18 |
| Ni-Re(OC6) | 5.03 | 0.08 | Ni-Nb(OC8) | 8.69 | 0.20 |
| Ni-Ti(OC7) | 6.65 | 0.19 | Ni-W(OC8) | 8.69 | 0.20 |
| Ni-Zr(OC7) | 6.65 | 0.13 | Ni-Re(OC8) | 8.69 | 0.20 |

**Table S7** DFT-calculated hydrogen adsorption free energies and corresponding doping distances of Ni–TM2@BN structures with favorable HER performance at different doping sites.

| H-TM2 | $d_{Ni-TM2}$ | $\triangle G_{H2*}$ | H-TM2 | $d_{Ni-TM2}$ | $\triangle G_{H2*}$ |
|---|---|---|---|---|---|
| Ni-Ti(OC1) | 2.52 | 0.13 | Ni-Fe(OC4) | 5.00 | -0.09 |
| Ni-Mn(OC1) | 2.52 | 0.01 | Ni-Ti(OC5) | 4.33 | 0.11 |
| Ni-Hf(OC1) | 2.52 | 0.006 | Ni-V(OC5) | 4.33 | 0.16 |
| Ni-Ti(OC2) | 2.57 | 0.07 | Ni-Cr(OC5) | 4.33 | -0.08 |
| Ni-Mn(OC2) | 2.57 | -0.04 | Ni-Mn(OC5) | 4.33 | -0.19 |
| Ni-Fe(OC2) | 2.57 | 0.18 | Ni-Mn(OC6) | 5.03 | -0.17 |
| Ni-Zr(OC2) | 2.57 | 0.099 | Ni-Co(OC6) | 5.03 | -0.03 |
| Ni-Rh(OC2) | 2.57 | 0.047 | Ni-Ru(OC6) | 5.03 | -0.09 |
| Ni-Pt(OC2) | 2.57 | -0.14 | Ni-Os(OC6) | 5.03 | 0.17 |
| Ni-Mn(OC3) | 4.37 | 0.14 | Ni-Sc(OC7) | 6.65 | -0.1 |
| Ni-Fe(OC3) | 4.37 | -0.17 | Ni-Co(OC7) | 6.65 | 0.17 |
| Ni-Zr(OC3) | 4.37 | -0.058 | Ni-Ru(OC7) | 6.65 | -0.12 |
| Ni-Pd(OC3) | 4.37 | 0.02 | Ni-Rh(OC7) | 6.65 | -0.06 |

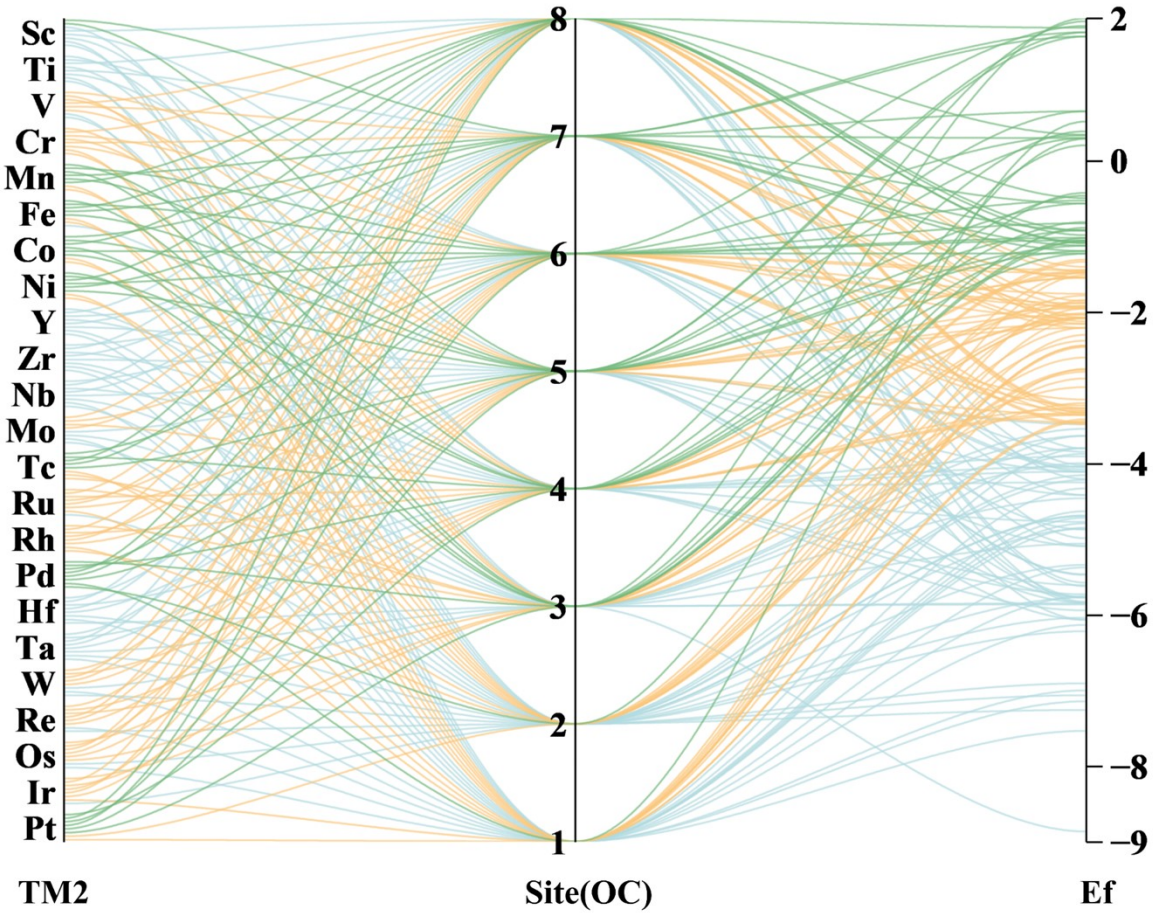


**Fig. S1** Formation energy ($E_f$) distribution plot of Ni–TM2 structures.

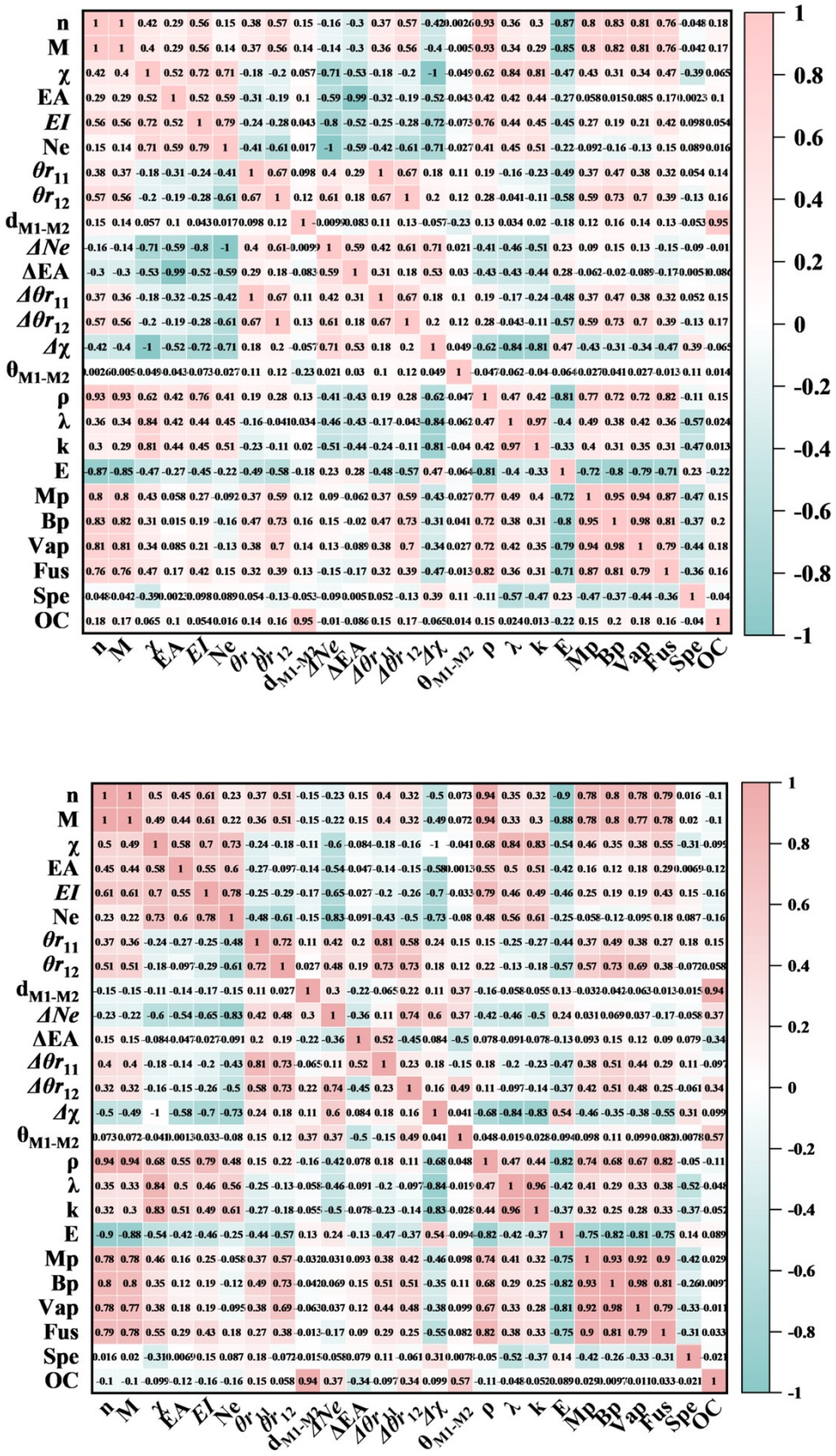


**Fig. S2** The correlations with the target values ($\triangle G_{H1*}$ and $\triangle G_{H2*}$) before feature preprocessing.

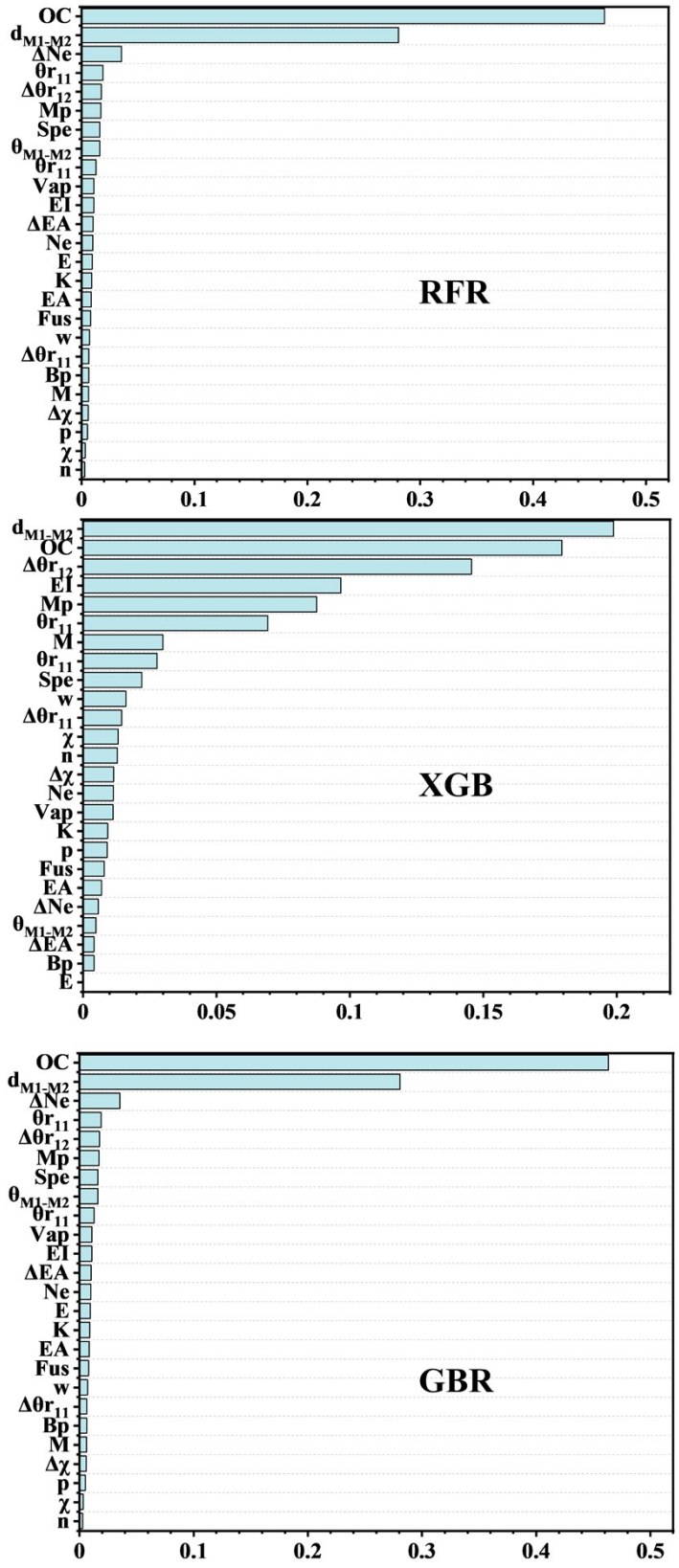


**Fig. S3** Feature importances of the three base models for the target value $\triangle G_{H1*}$.

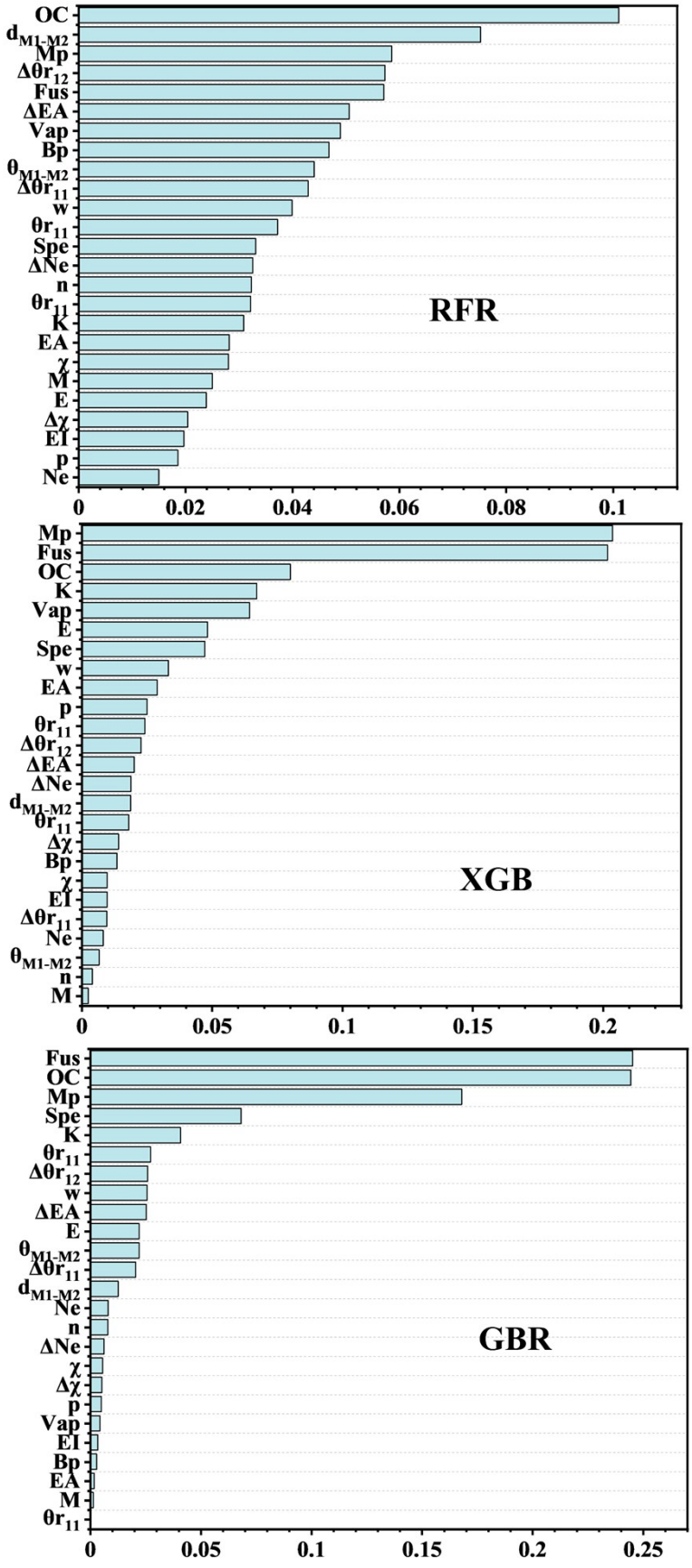


**Fig. S4** Feature importances of the three base models for the target value $\triangle G_{H2*}$.

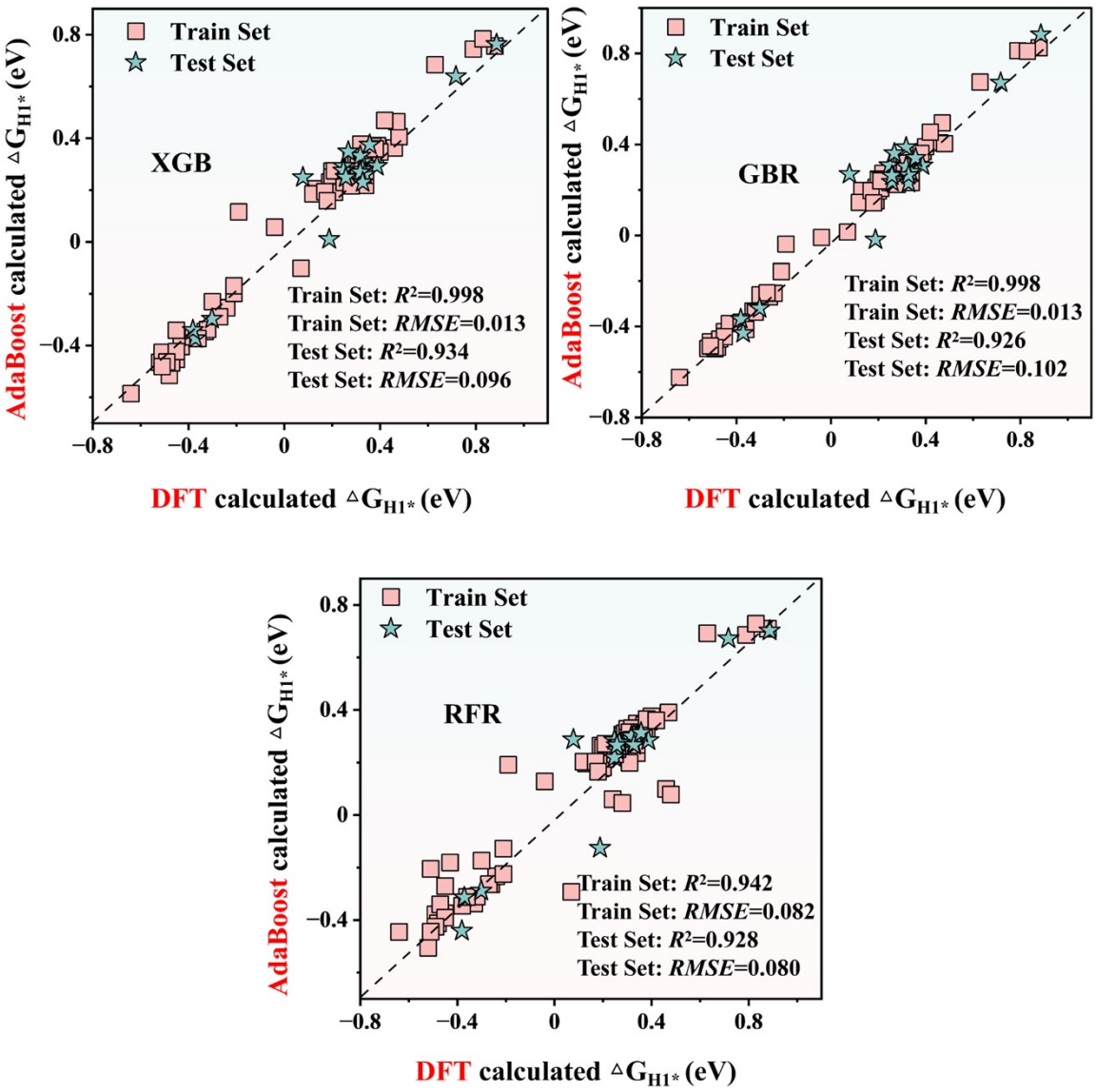


**Fig. S5** Prediction accuracies of the three base models on the $\triangle G_{H1*}$ dataset after feature preprocessing.

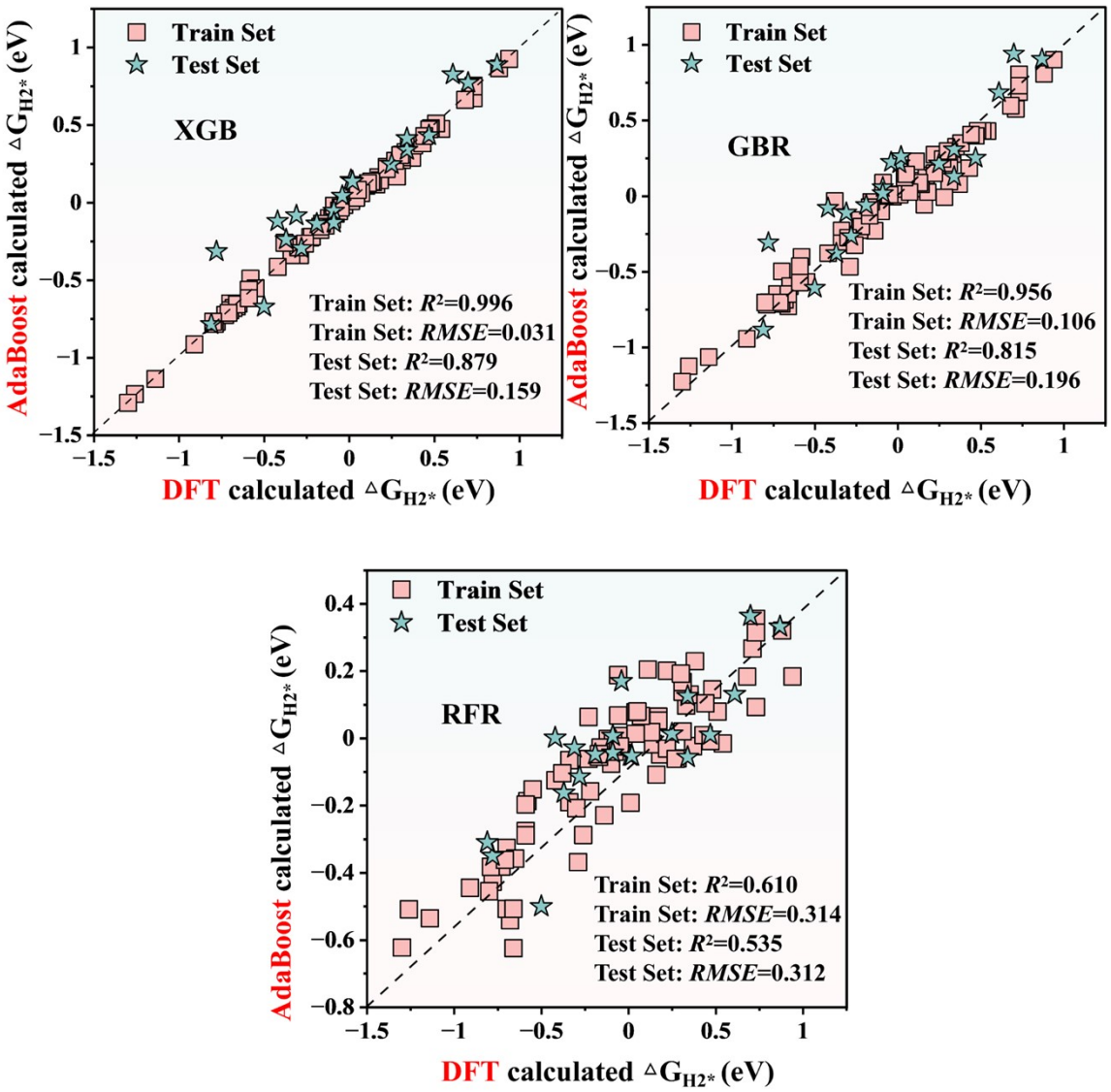


**Fig. S6** Prediction accuracies of the three base models on the $\triangle G_{H2^*}$ dataset after feature preprocessing.

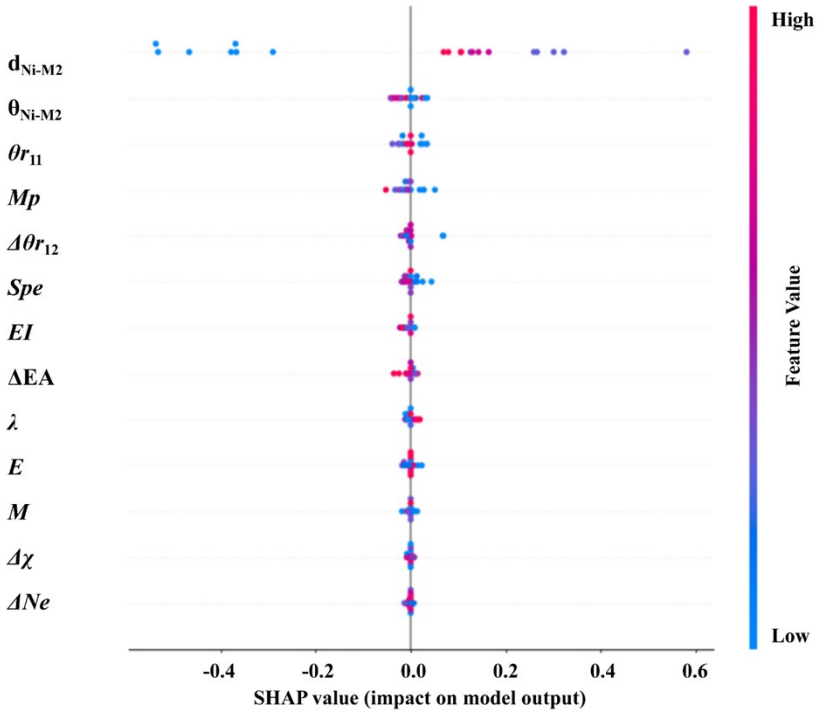


**Fig. S7** SHAP analysis of AdaBoost–GBR ($\triangle G_{H1*}$).

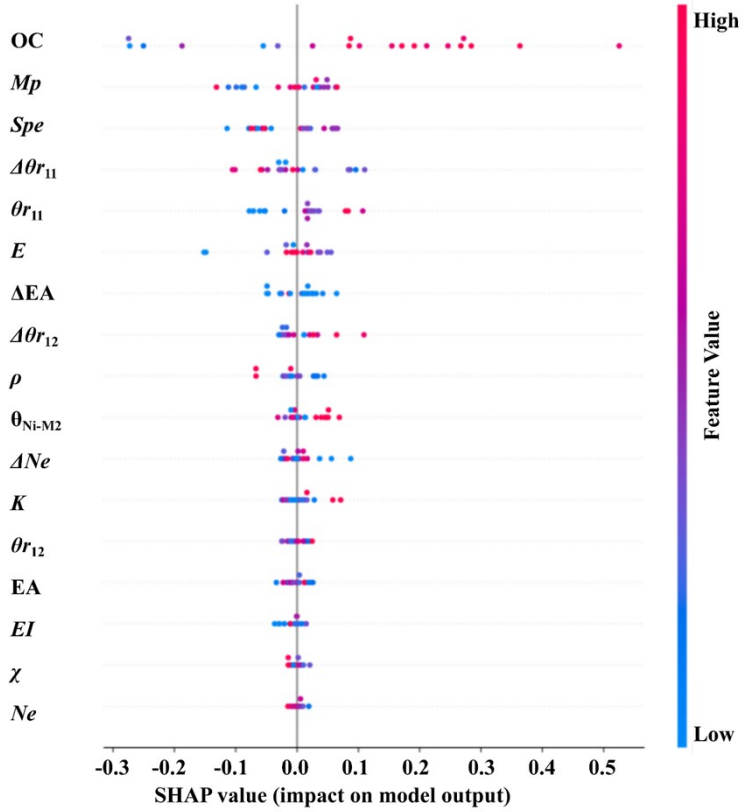


**Fig. S8** SHAP analysis of AdaBoost–GBR ($\triangle G_{H2*}$).

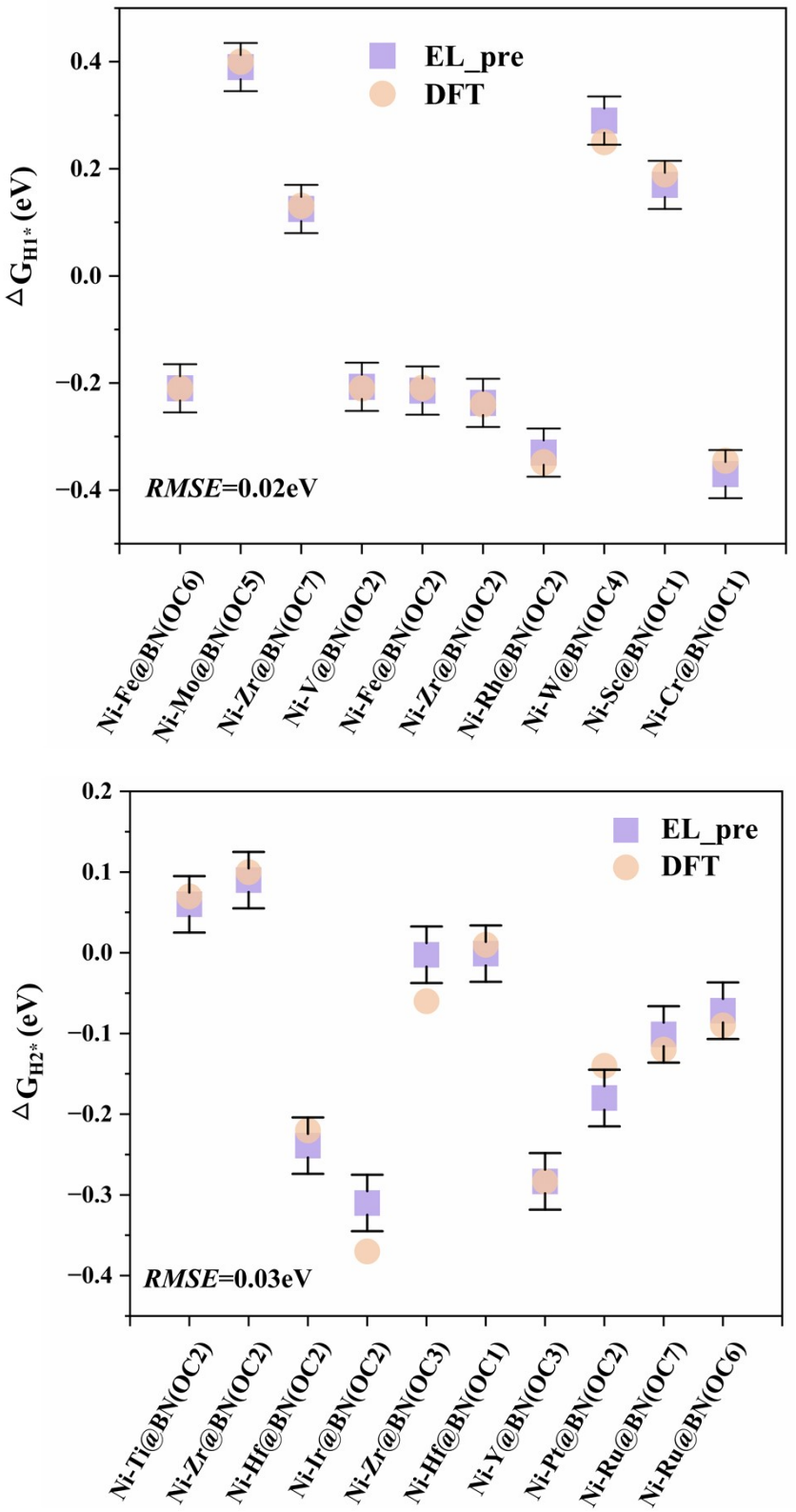


**Fig. S9** Error plots between the predicted values of AdaBoost GBR($\triangle G_{H1*}$) and AdaBoost GBR ($\triangle G_{H2*}$) and the DFT-calculated values.

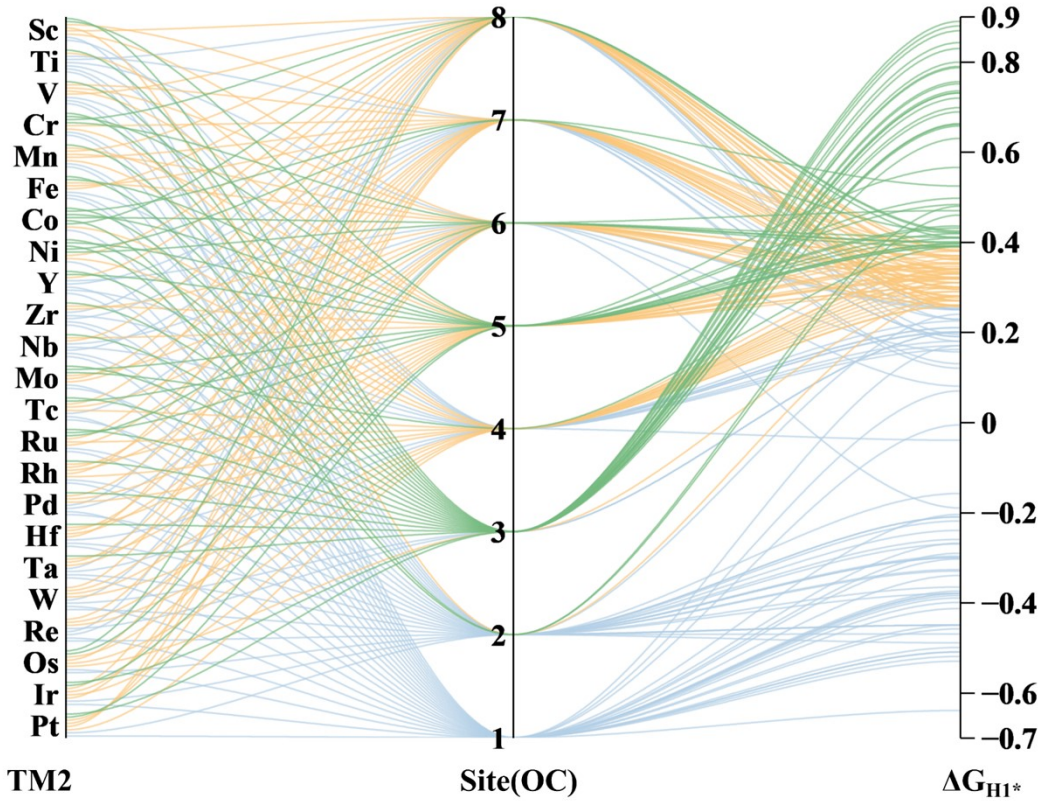


**Fig. S10** Data distribution plot of $\triangle G_{H1*}$ values from DFT calculations and EL predictions across eight TM2 doping sites.

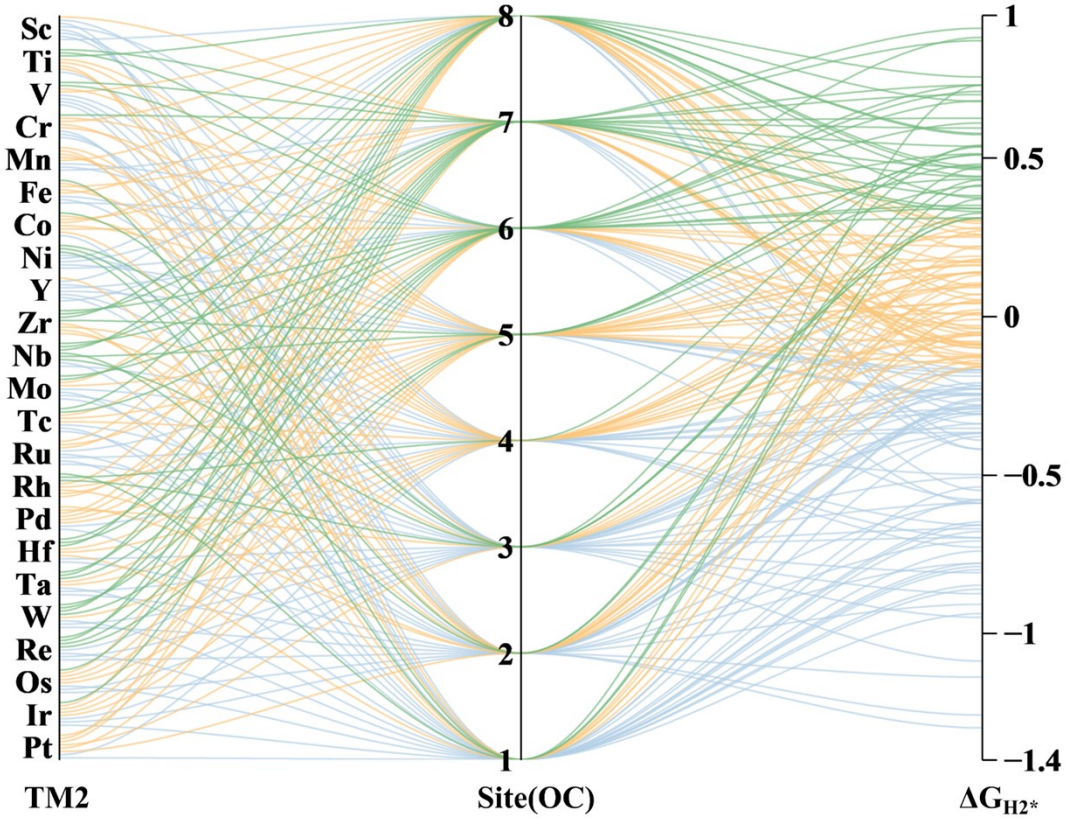


**Fig. S11** Data distribution plot of $\triangle G_{H2*}$ values from DFT calculations and EL predictions across eight TM2 doping sites.

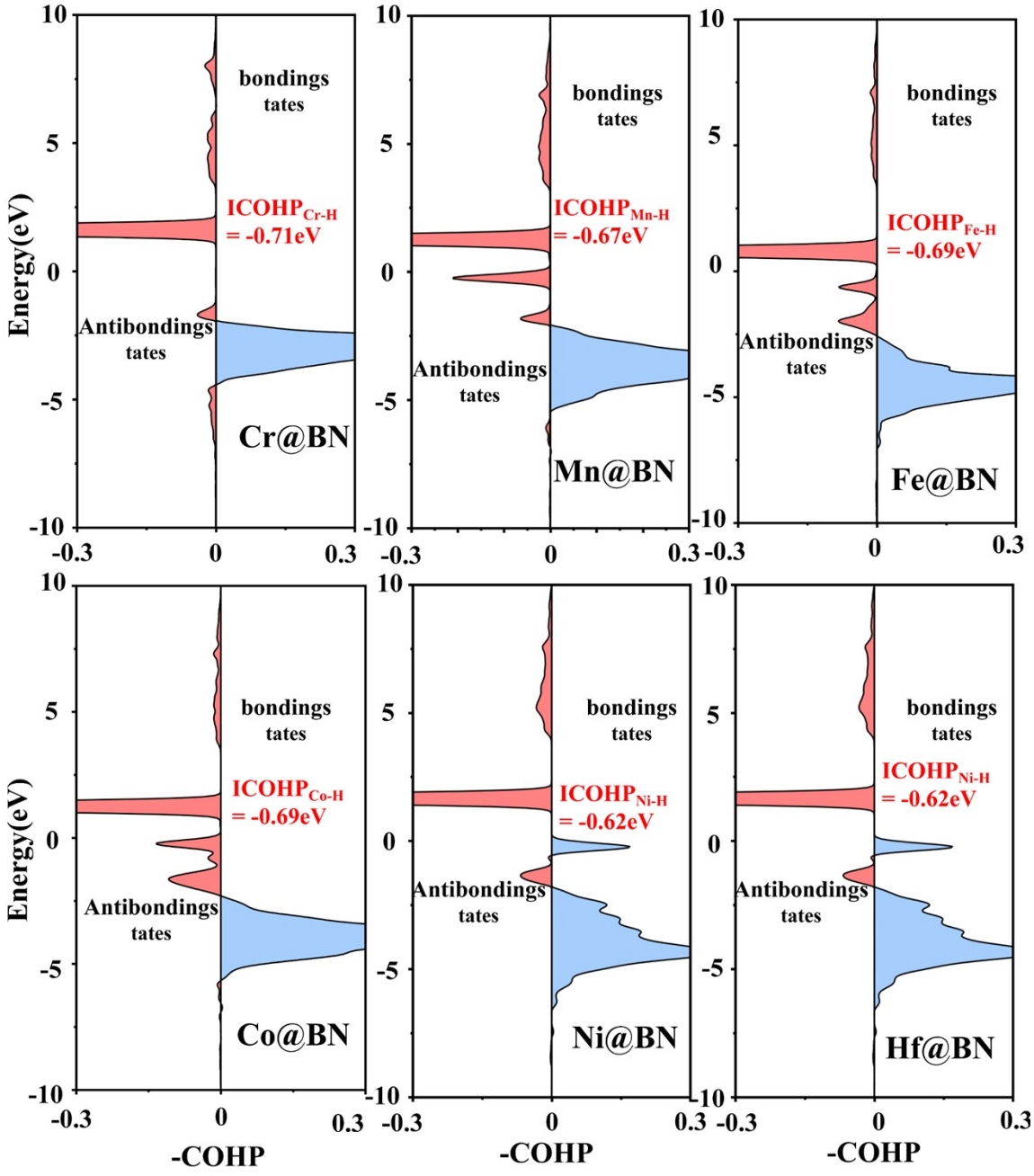
Energy(eV)
10
5
0
-5
-10
-0.3
0
0.3
-COHP
bondings tates
Antibondings tates
ICOHP$_{Cr-H}$ = -0.71eV
Cr@BN
ICOHP$_{Mn-H}$ = -0.67eV
Mn@BN
ICOHP$_{Fe-H}$ = -0.69eV
Fe@BN
ICOHP$_{Co-H}$ = -0.69eV
Co@BN
ICOHP$_{Ni-H}$ = -0.62eV
Ni@BN
Hf@BN

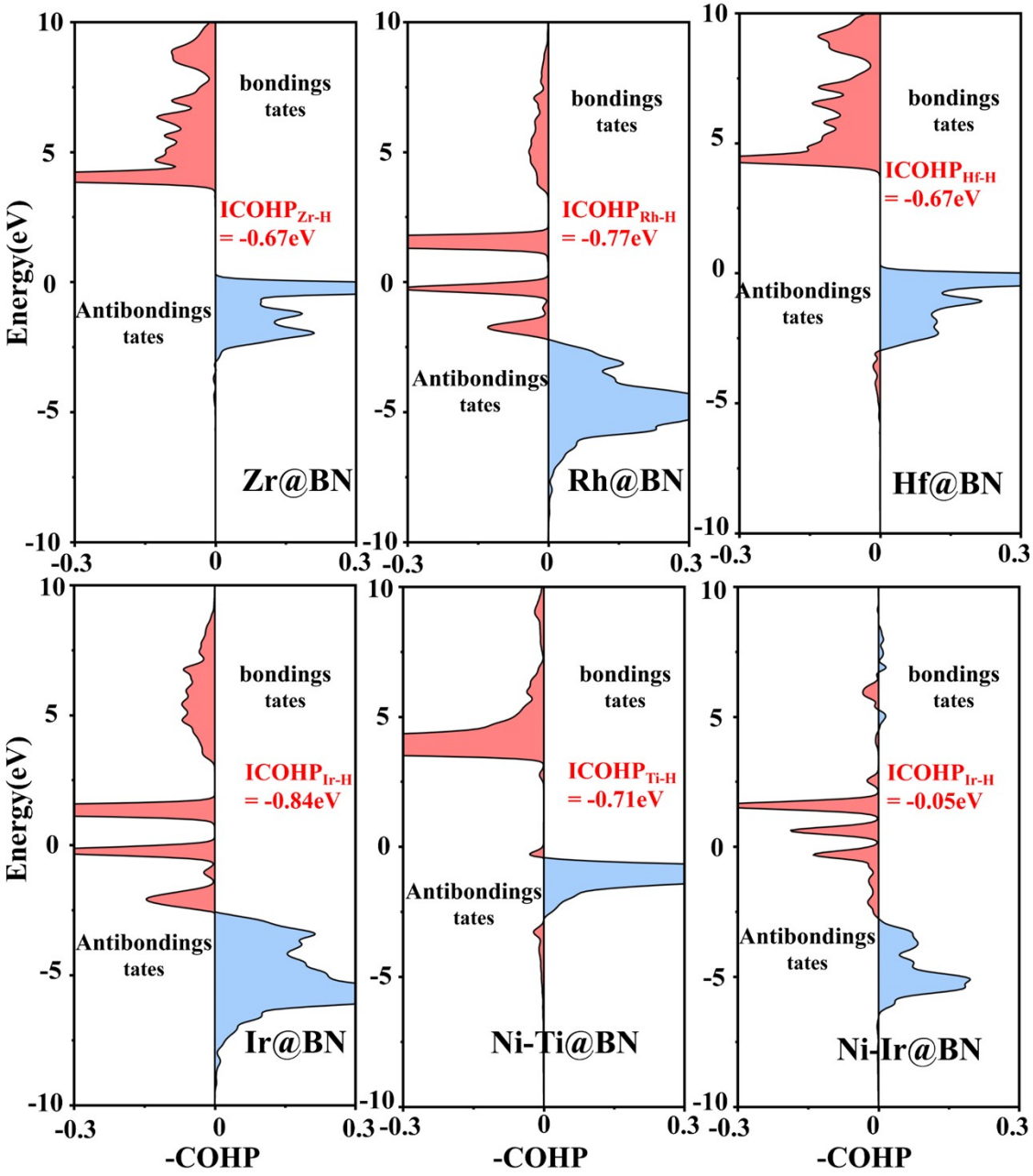
Energy(eV)
10
5
0
-5
-10
-0.3
0
0.3
-COHP
bondings tates
Antibondings tates
ICOHP$_{Zr-H}$ = -0.67eV
Zr@BN
ICOHP$_{Rh-H}$ = -0.77eV
Rh@BN
ICOHP$_{Hf-H}$ = -0.67eV
Hf@BN
ICOHP$_{Ir-H}$ = -0.84eV
Ir@BN
ICOHP$_{Ti-H}$ = -0.71eV
Ni-Ti@BN
ICOHP$_{Ir-H}$ = -0.05eV
Ni-Ir@BN

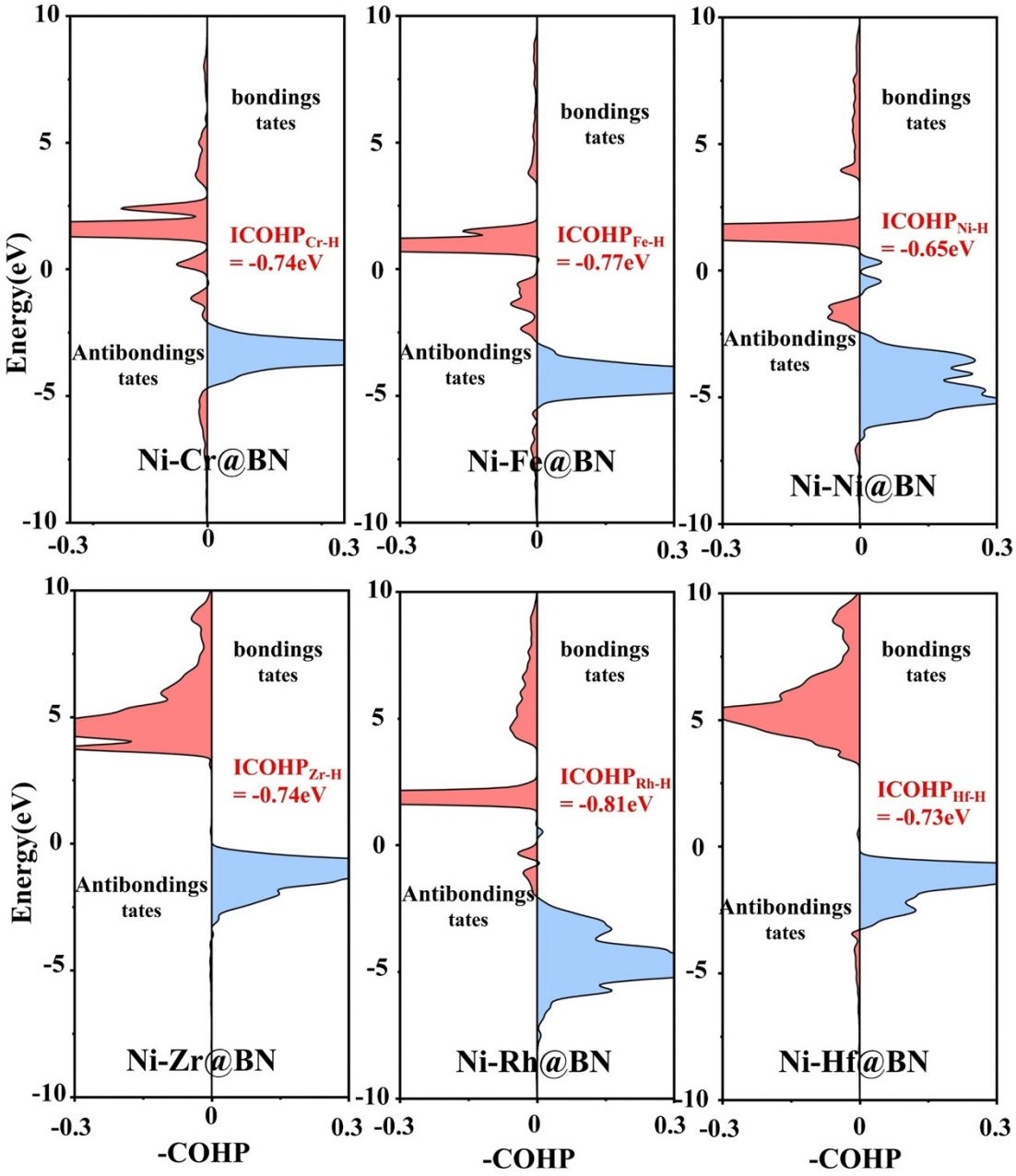


**Fig. S12** COHP calculations for randomly selected single-metal-doped and bimetal-doped BN structures.

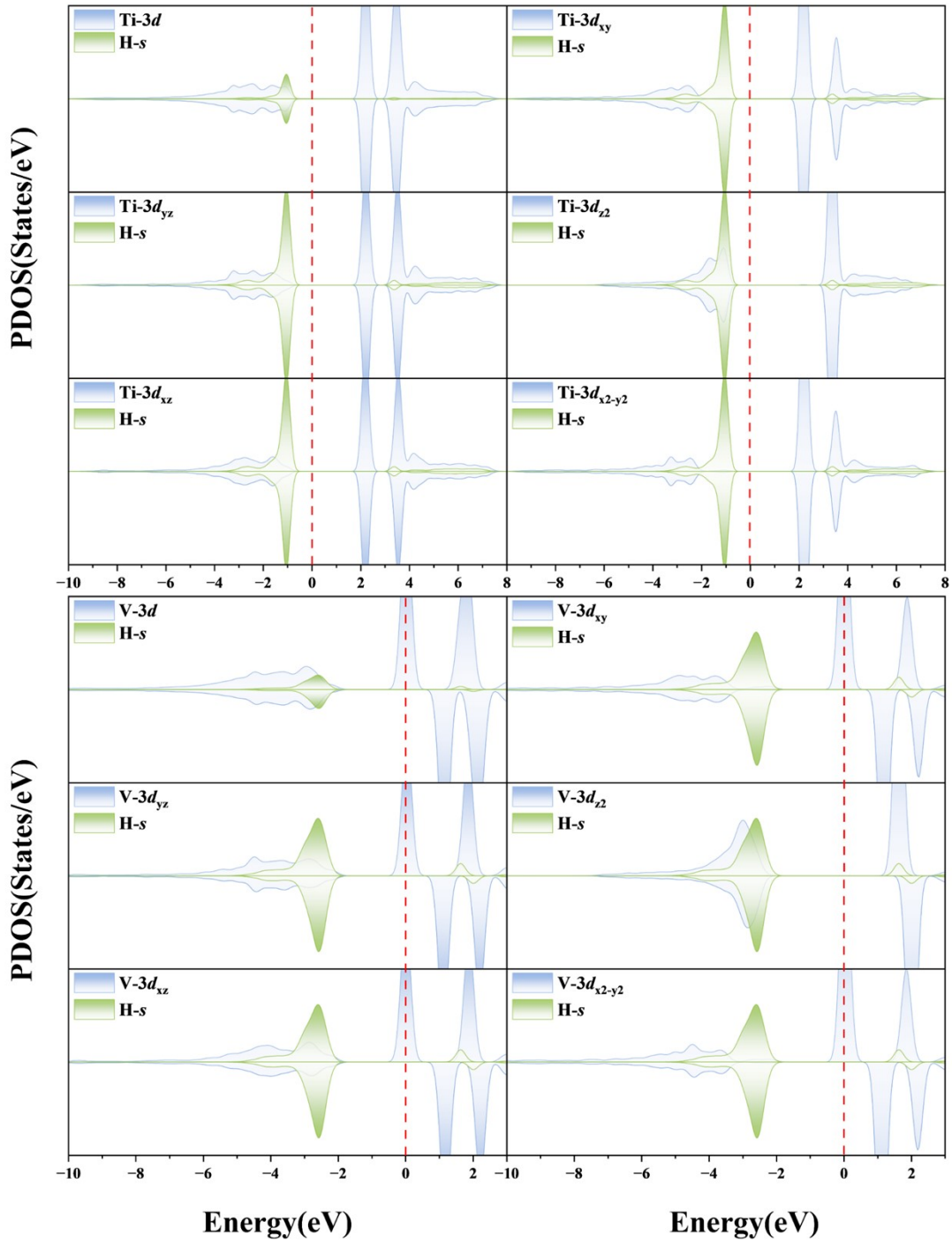
Ti-3d
H-s
Ti-3dxy
H-s
Ti-3dyz
H-s
Ti-3dz2
H-s
Ti-3dxz
H-s
Ti-3dx2-y2
H-s
V-3d
H-s
V-3dxy
H-s
V-3dyz
H-s
V-3dz2
H-s
V-3dxz
H-s
V-3dx2-y2
H-s
PDOS(States/eV)
PDOS(States/eV)
Energy(eV)
Energy(eV)

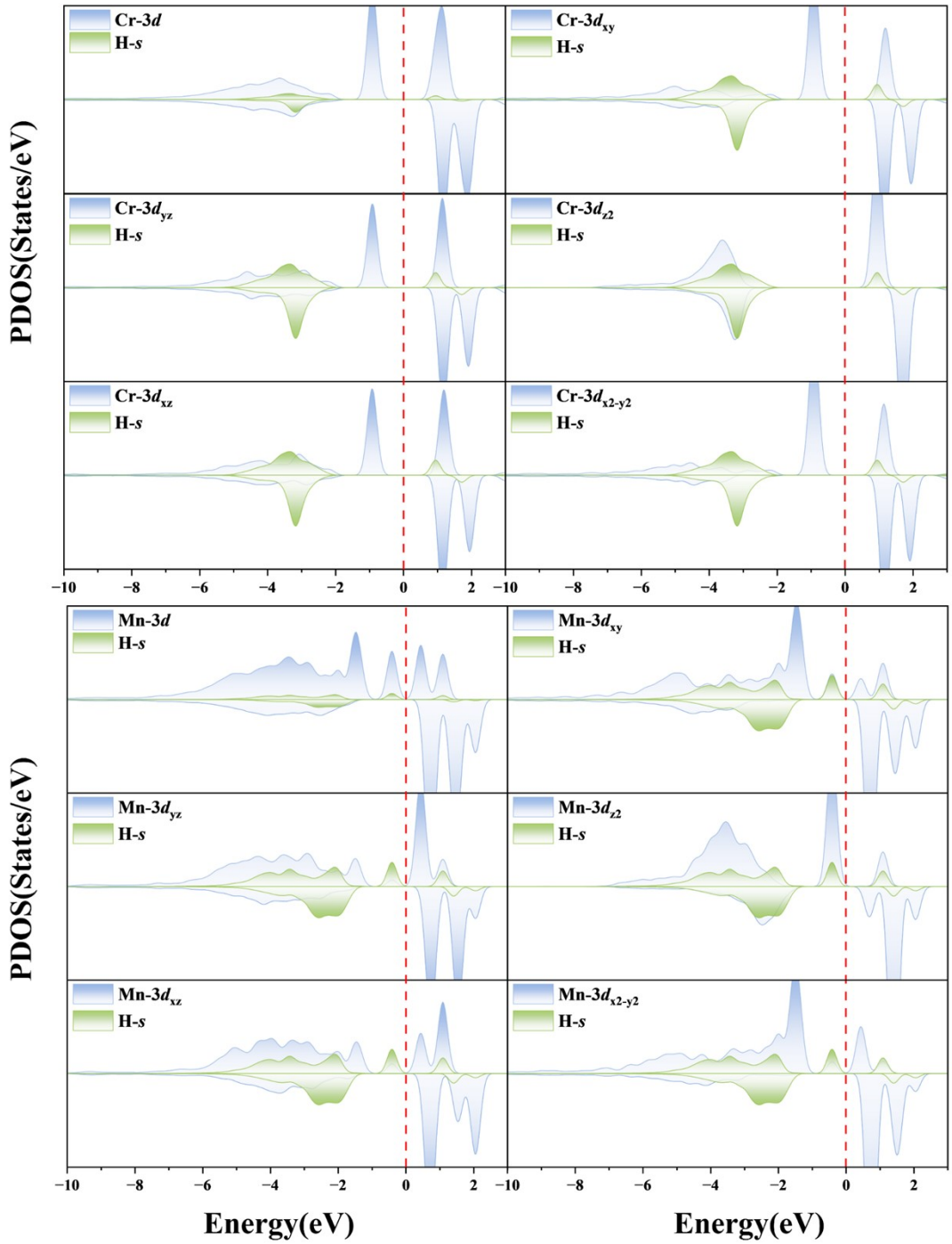
PDOS(States/eV)
Cr-3d
H-s
Cr-3d_xy
H-s
Cr-3d_yz
H-s
Cr-3d_z2
H-s
Cr-3d_xz
H-s
Cr-3d_x2-y2
H-s
−10 −8 −6 −4 −2 0 2
PDOS(States/eV)
Mn-3d
H-s
Mn-3d_xy
H-s
Mn-3d_yz
H-s
Mn-3d_z2
H-s
Mn-3d_xz
H-s
Mn-3d_x2-y2
H-s
−10 −8 −6 −4 −2 0 2
Energy(eV)
Energy(eV)

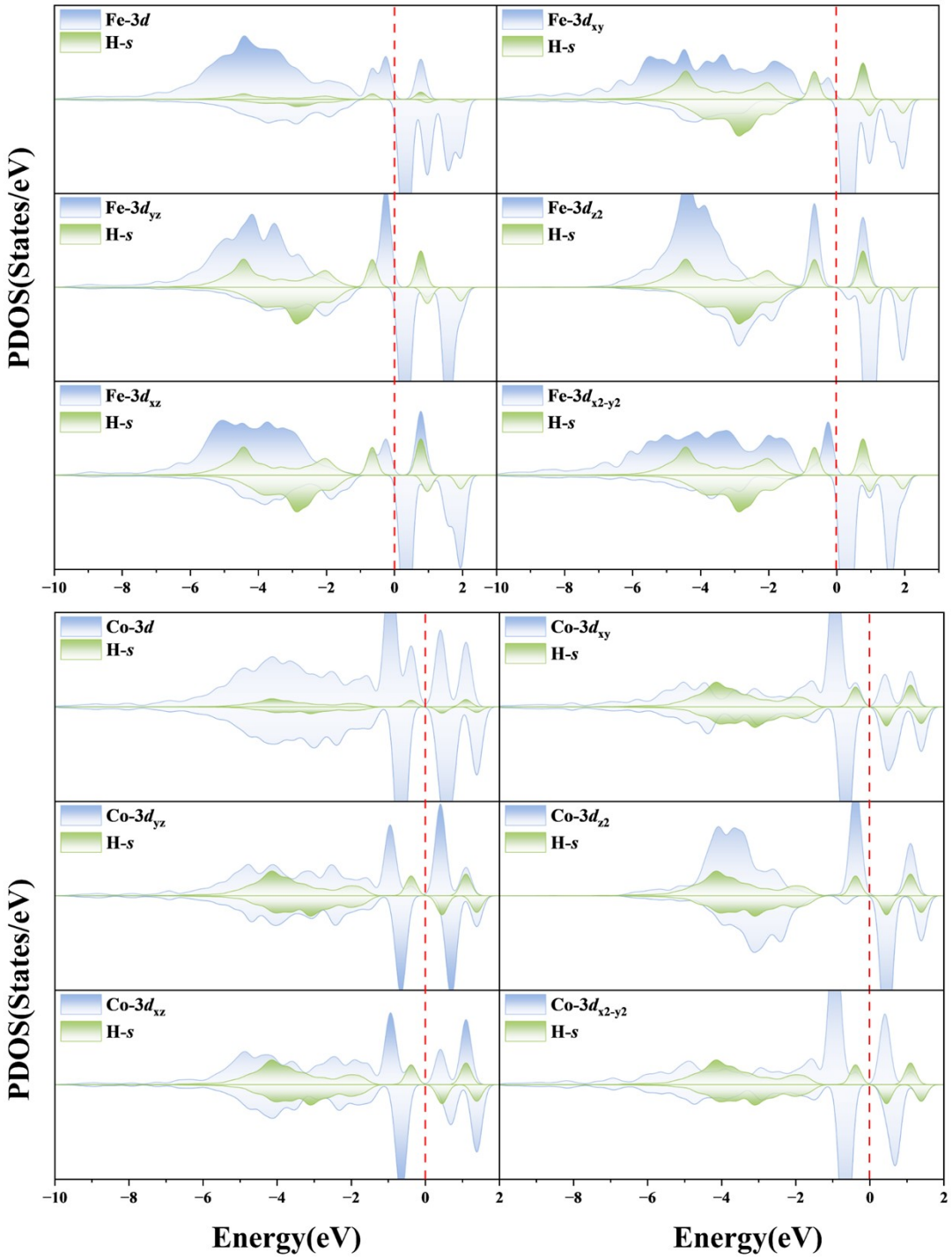
Fe-3d
H-s
Fe-3d$_{xy}$
H-s
Fe-3d$_{yz}$
H-s
Fe-3d$_{z2}$
H-s
Fe-3d$_{xz}$
H-s
Fe-3d$_{x2-y2}$
H-s
Co-3d
H-s
Co-3d$_{xy}$
H-s
Co-3d$_{yz}$
H-s
Co-3d$_{z2}$
H-s
Co-3d$_{xz}$
H-s
Co-3d$_{x2-y2}$
H-s
PDOS(States/eV)
PDOS(States/eV)
−10 −8 −6 −4 −2 0 2
Energy(eV)
Energy(eV)

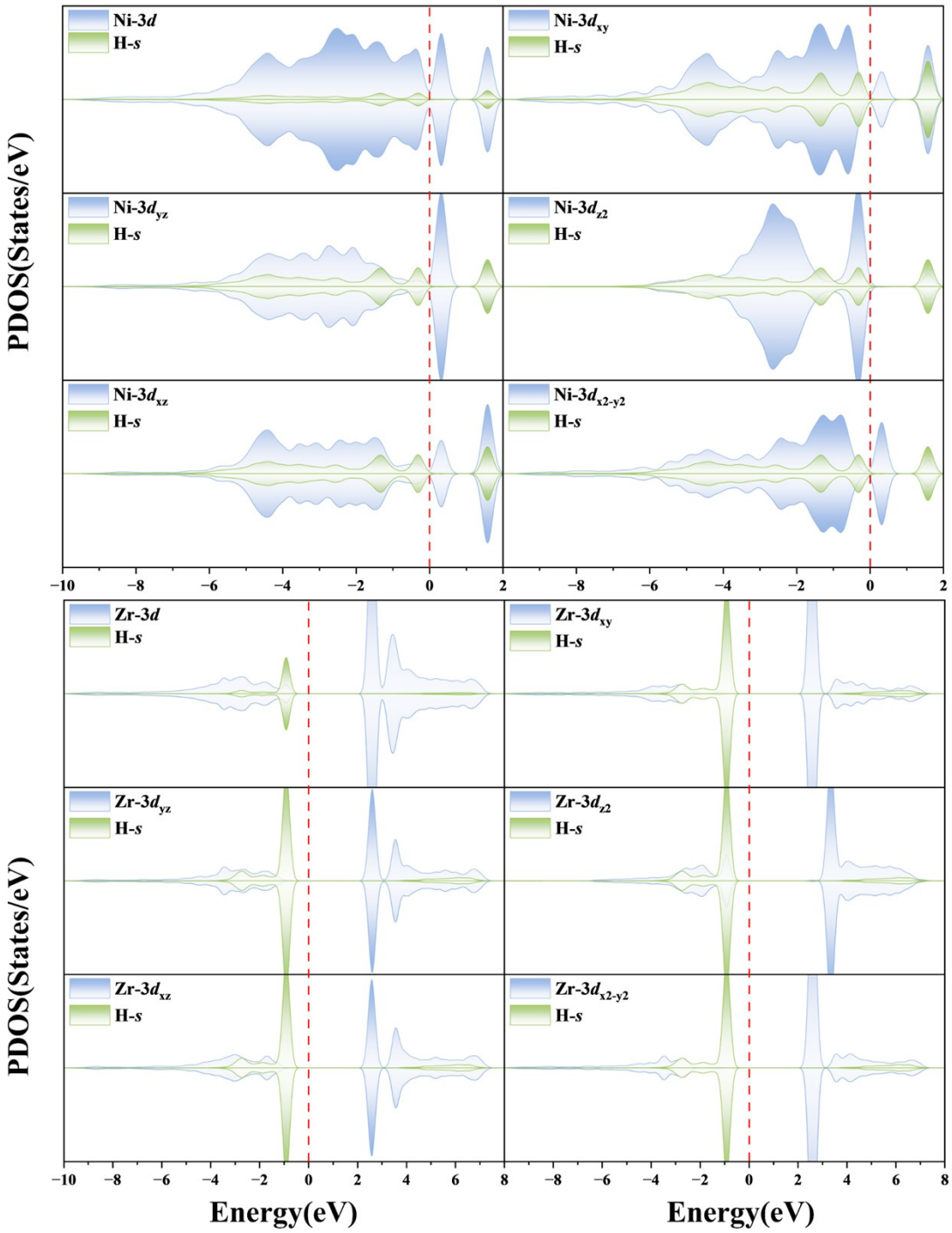
Ni-3d
H-s
Ni-3d$_{xy}$
Ni-3d$_{yz}$
Ni-3d$_{z2}$
Ni-3d$_{xz}$
Ni-3d$_{x2-y2}$
Zr-3d
Zr-3d$_{xy}$
Zr-3d$_{yz}$
Zr-3d$_{z2}$
Zr-3d$_{xz}$
Zr-3d$_{x2-y2}$
PDOS(States/eV)
PDOS(States/eV)
Energy(eV)
Energy(eV)

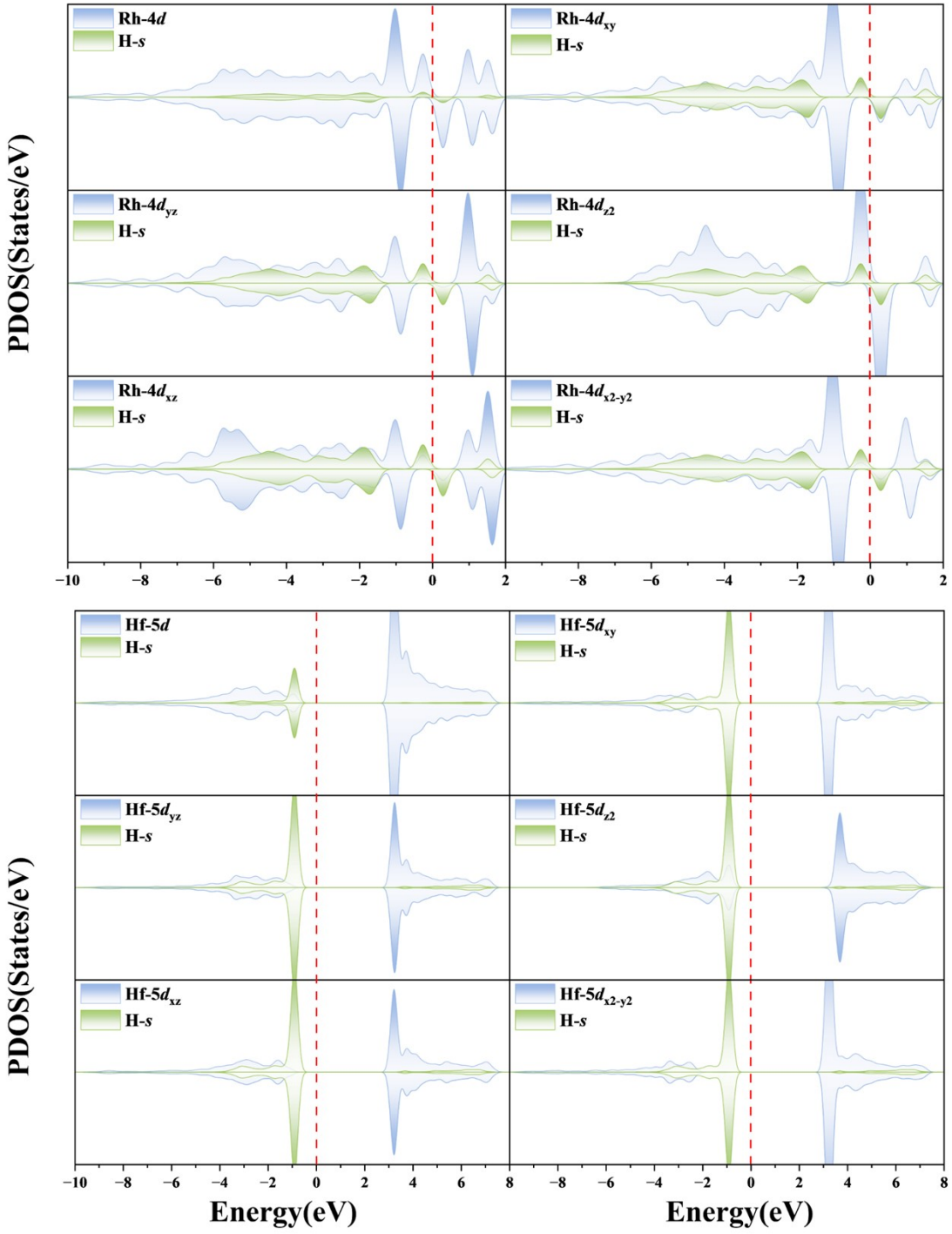
Rh-4d
H-s
Rh-4d_xy
H-s
Rh-4d_yz
H-s
Rh-4d_z2
H-s
Rh-4d_xz
H-s
Rh-4d_x2-y2
H-s
PDOS(States/eV)
Hf-5d
H-s
Hf-5d_xy
H-s
Hf-5d_yz
H-s
Hf-5d_z2
H-s
Hf-5d_xz
H-s
Hf-5d_x2-y2
H-s
PDOS(States/eV)
Energy(eV)
Energy(eV)

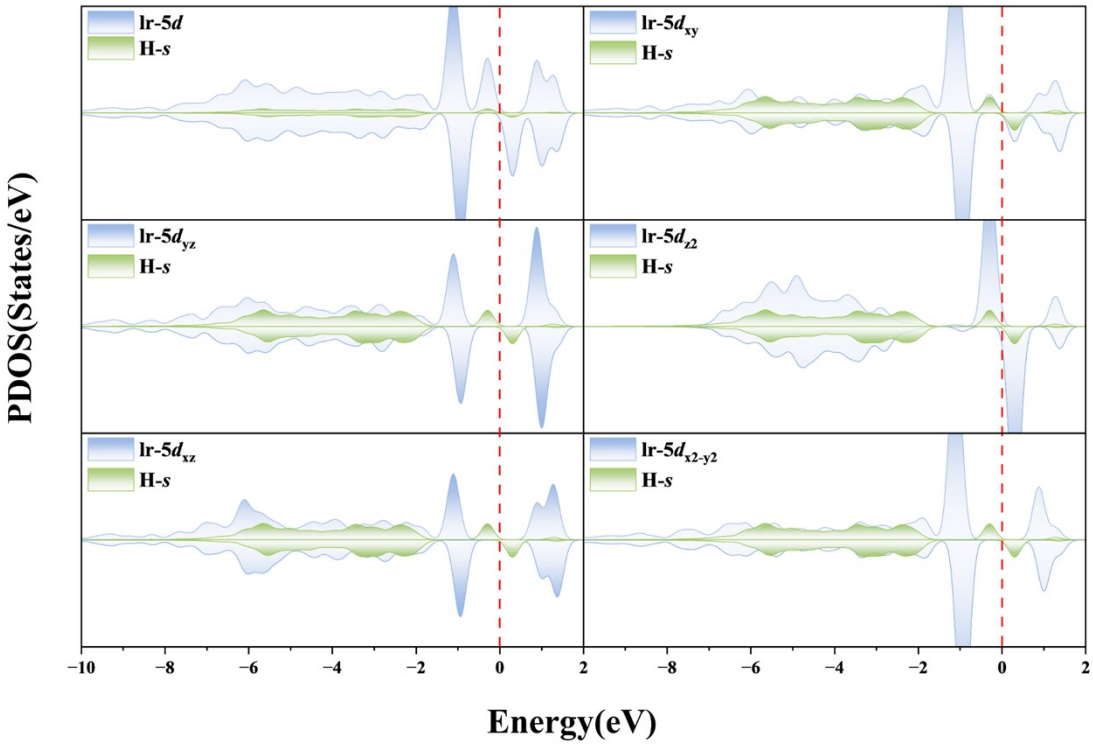


**Fig. S13** PDOS plots for randomly selected single-metal-doped BN structures.

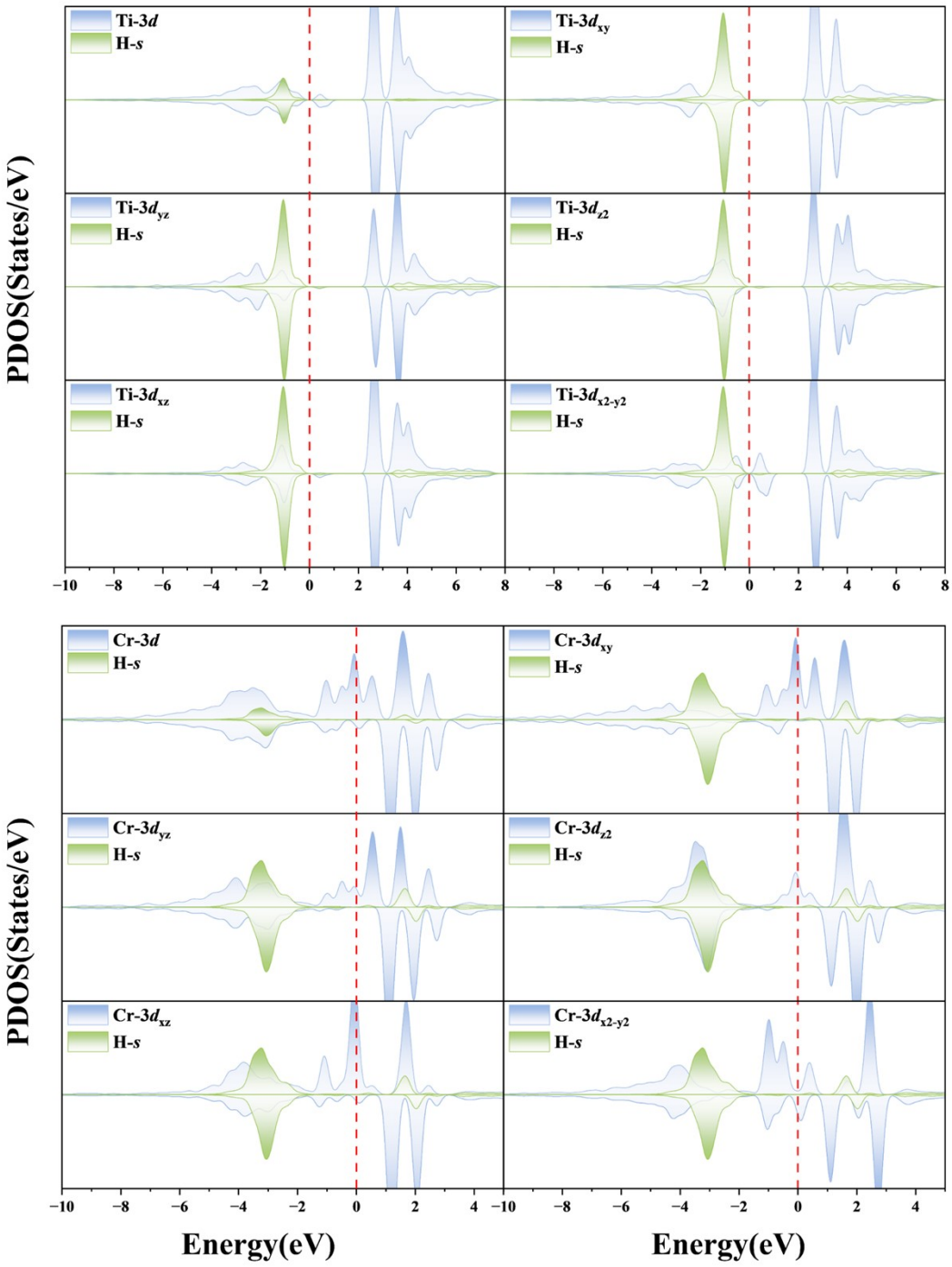
Ti-3d
H-s
Ti-3d_xy
H-s
Ti-3d_yz
H-s
Ti-3d_z2
H-s
Ti-3d_xz
H-s
Ti-3d_x2-y2
H-s
PDOS(States/eV)
Cr-3d
H-s
Cr-3d_xy
H-s
Cr-3d_yz
H-s
Cr-3d_z2
H-s
Cr-3d_xz
H-s
Cr-3d_x2-y2
H-s
PDOS(States/eV)
Energy(eV)
Energy(eV)

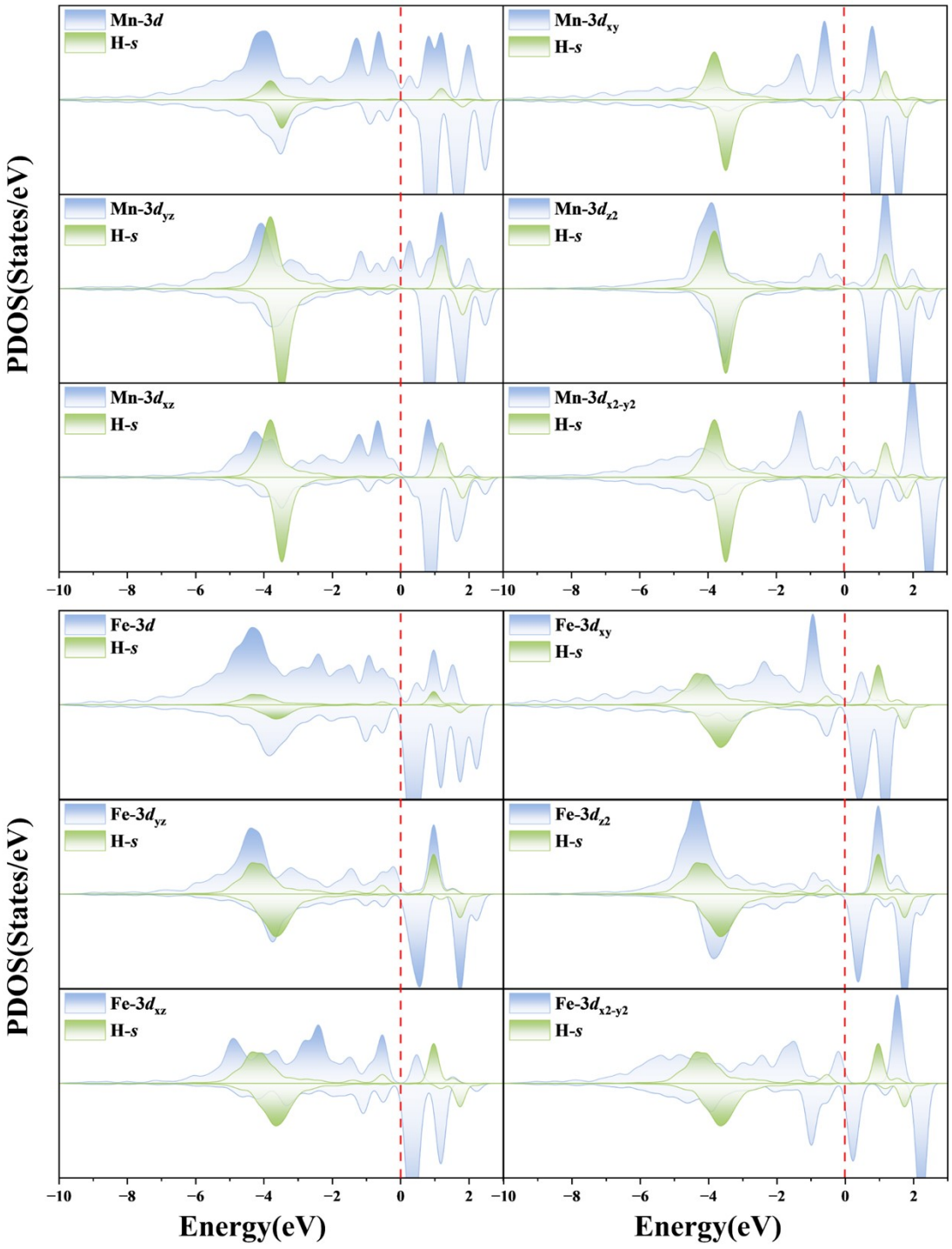
Mn-3d
H-s
Mn-3d$_{xy}$
H-s
Mn-3d$_{yz}$
H-s
Mn-3d$_{z2}$
H-s
Mn-3d$_{xz}$
H-s
Mn-3d$_{x2-y2}$
H-s
Fe-3d
H-s
Fe-3d$_{xy}$
H-s
Fe-3d$_{yz}$
H-s
Fe-3d$_{z2}$
H-s
Fe-3d$_{xz}$
H-s
Fe-3d$_{x2-y2}$
H-s
PDOS(States/eV)
PDOS(States/eV)
−10
−8
−6
−4
−2
0
2
Energy(eV)
Energy(eV)

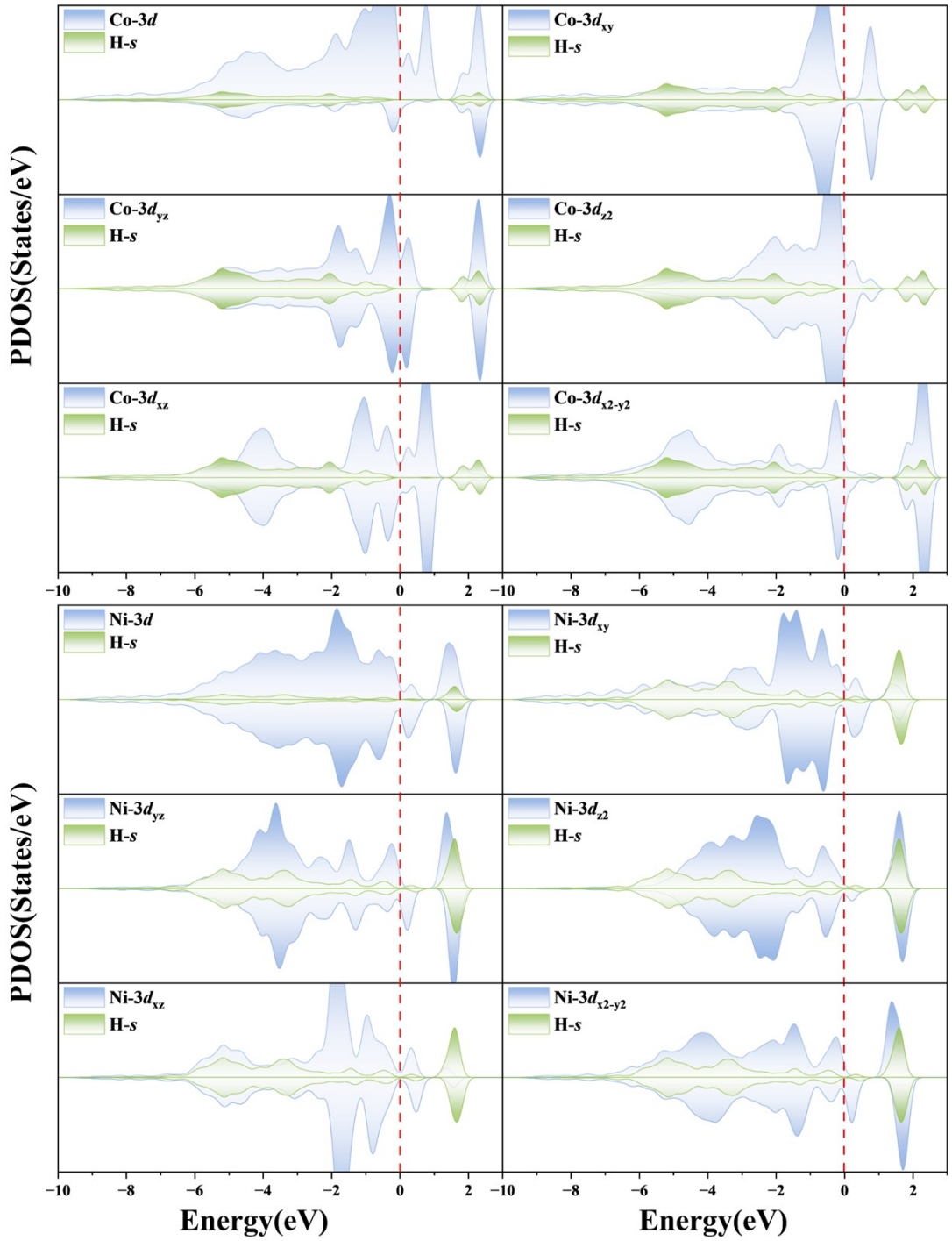
Co-3d
H-s
Co-3d$_{xy}$
H-s
Co-3d$_{yz}$
H-s
Co-3d$_{z2}$
H-s
Co-3d$_{xz}$
H-s
Co-3d$_{x2-y2}$
H-s
PDOS(States/eV)
Ni-3d
H-s
Ni-3d$_{xy}$
H-s
Ni-3d$_{yz}$
H-s
Ni-3d$_{z2}$
H-s
Ni-3d$_{xz}$
H-s
Ni-3d$_{x2-y2}$
H-s
PDOS(States/eV)
−10 −8 −6 −4 −2 0 2
Energy(eV)
Energy(eV)

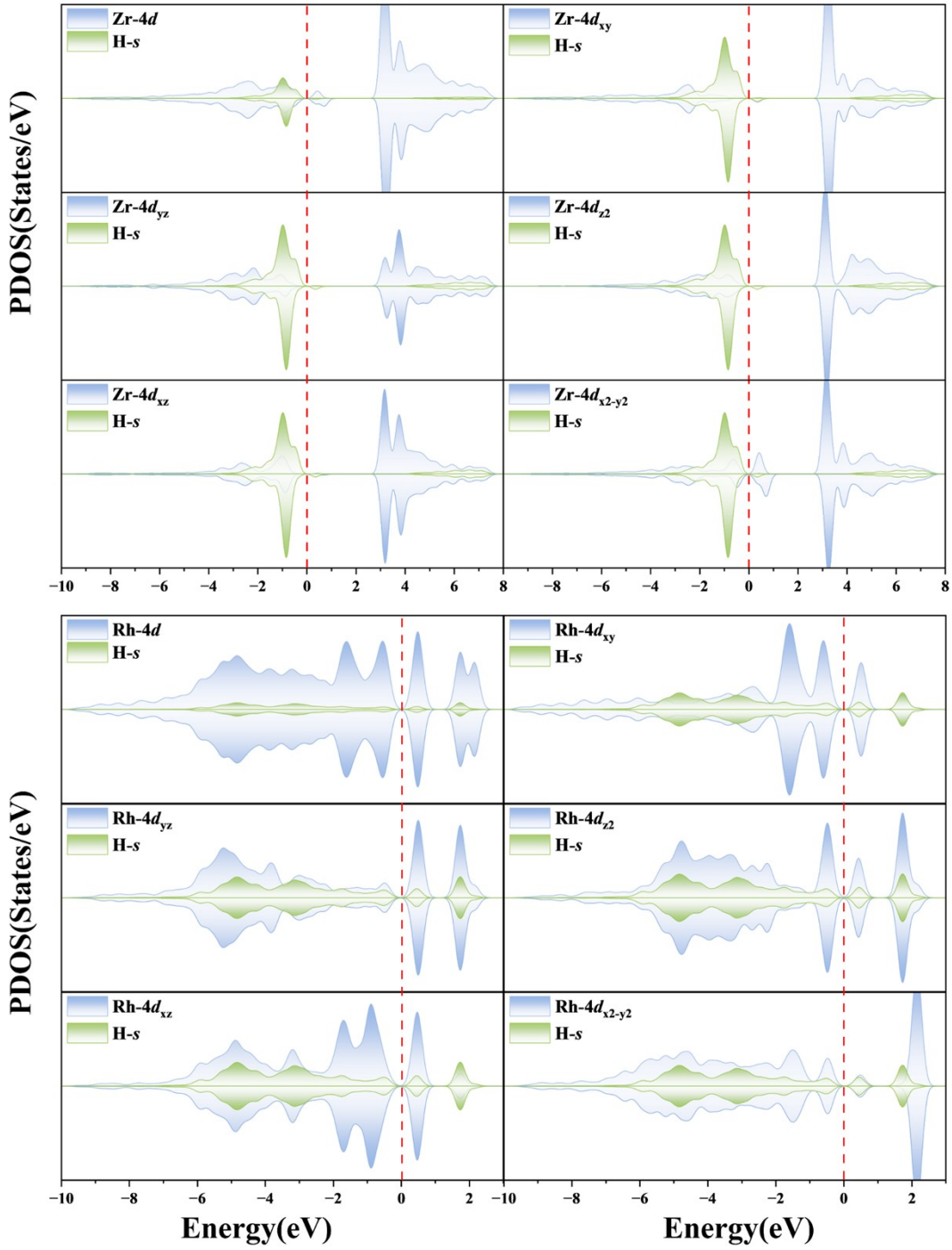
PDOS(States/eV)
Zr-4d
H-s
Zr-4d$_{xy}$
Zr-4d$_{yz}$
Zr-4d$_{z2}$
Zr-4d$_{xz}$
Zr-4d$_{x2-y2}$
Rh-4d
Rh-4d$_{xy}$
Rh-4d$_{yz}$
Rh-4d$_{z2}$
Rh-4d$_{xz}$
Rh-4d$_{x2-y2}$
Energy(eV)

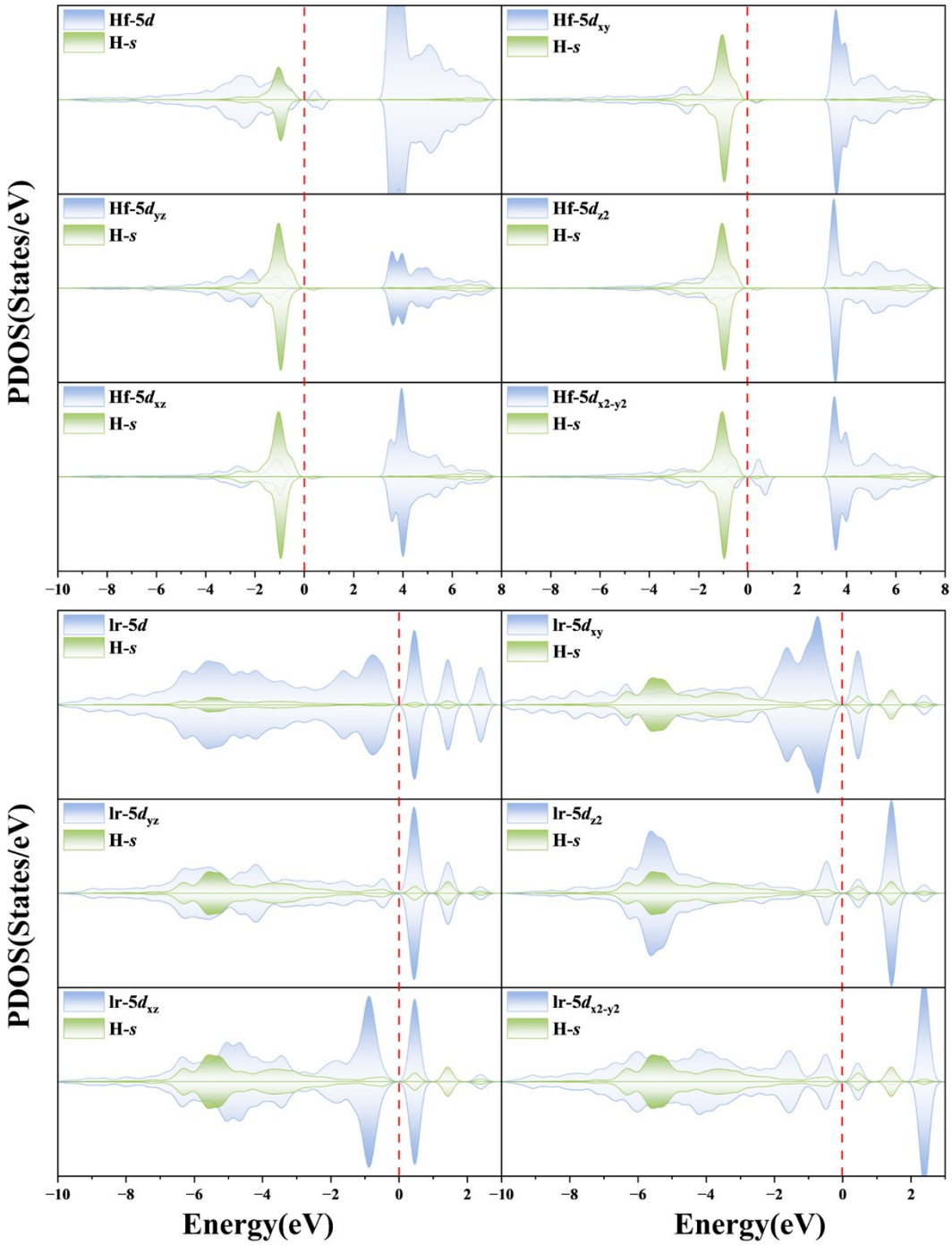


**Fig. S14** PDOS plots for randomly selected bimetal-doped BN structures.

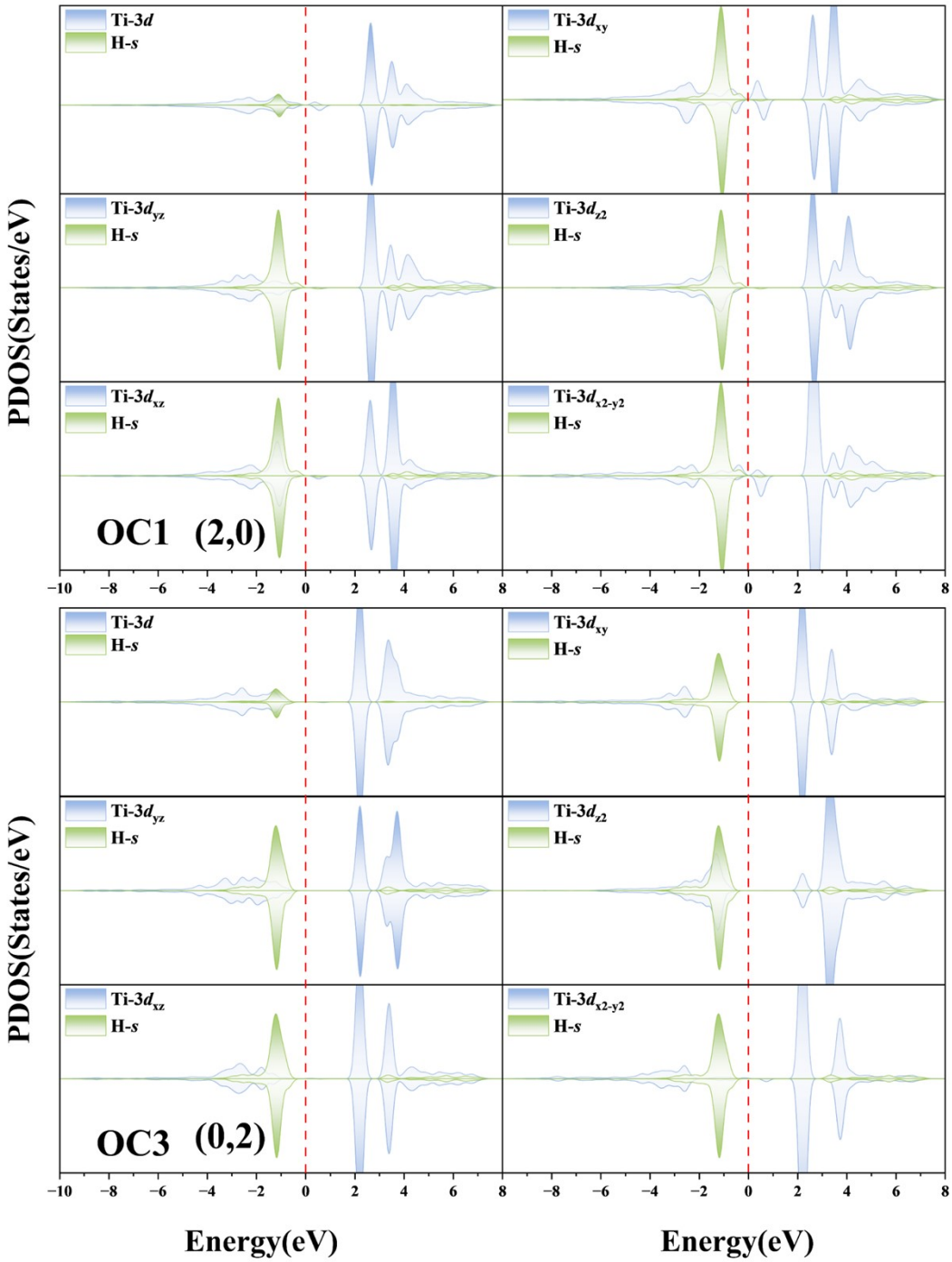
Ti-3d
H-s
Ti-3d_xy
Ti-3d_yz
Ti-3d_z2
Ti-3d_xz
Ti-3d_x2-y2
OC1 (2,0)
OC3 (0,2)
PDOS(States/eV)
Energy(eV)
−10 −8 −6 −4 −2 0 2 4 6 8

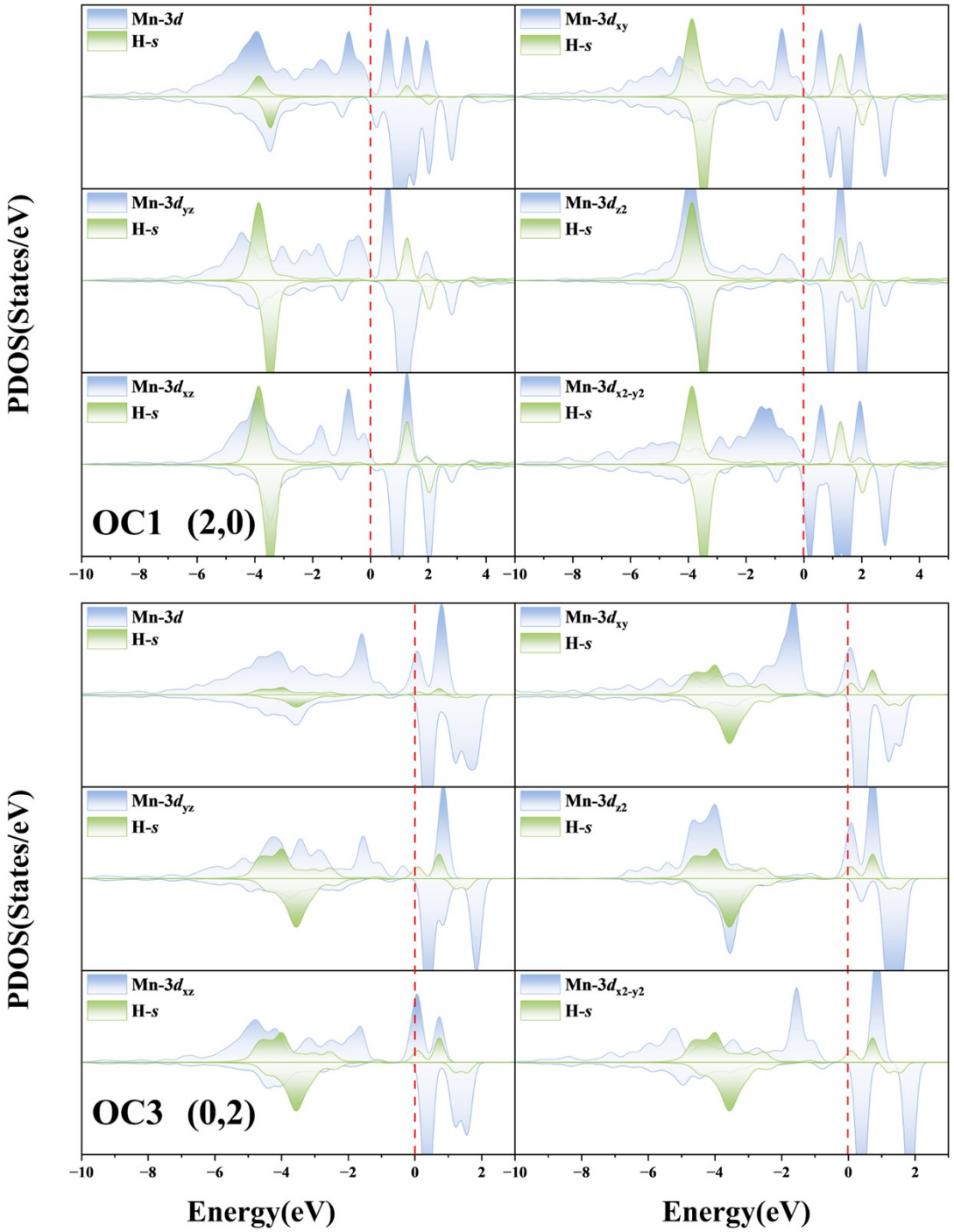


**Fig. S15** PDOS plots for the Ni- and Mn-doped OC1 and OC3 configurations.

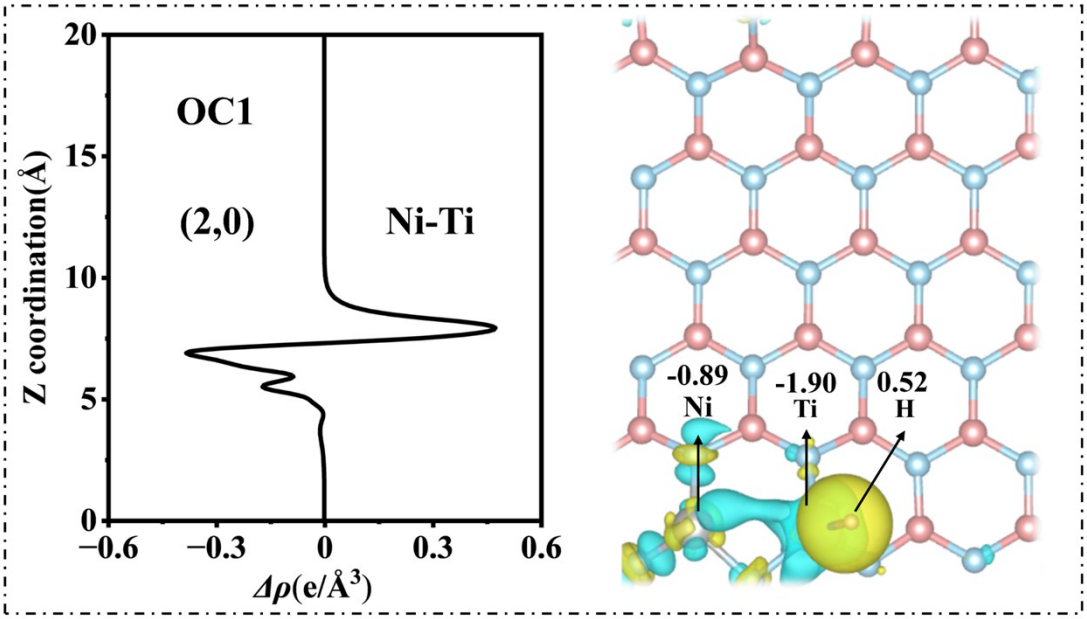
OC1
(2,0)
Ni-Ti
Z coordination(Å)
20
15
10
5
0
−0.6
−0.3
0
0.3
0.6
Δρ(e/Å³)
-0.89
Ni
-1.90
Ti
0.52
H

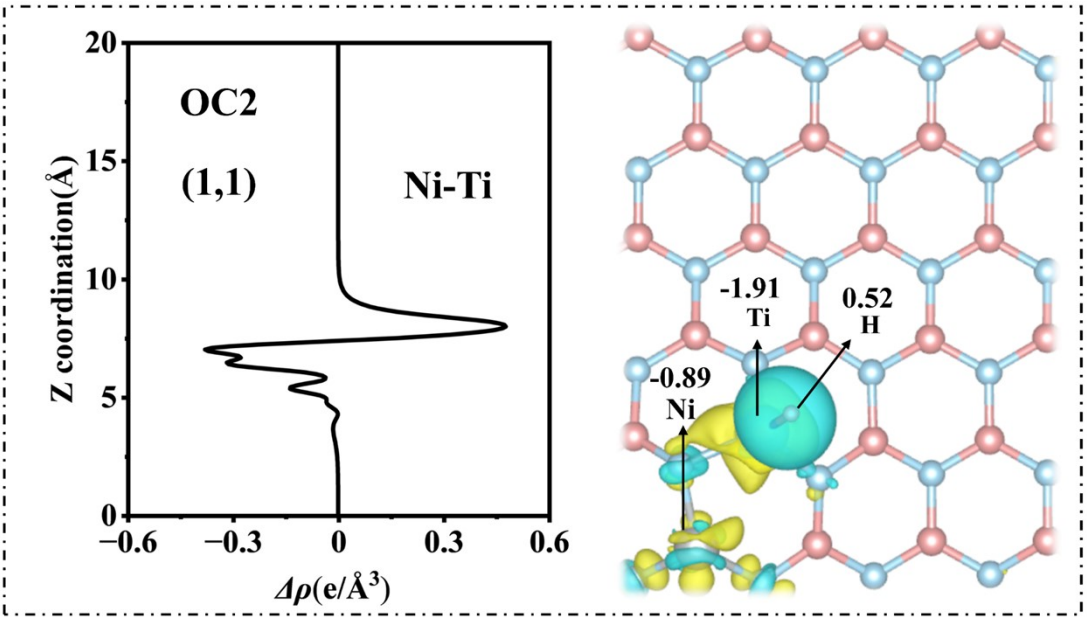
OC2
(1,1)
Ni-Ti
Z coordination(Å)
20
15
10
5
0
−0.6
−0.3
0
0.3
0.6
Δρ(e/Å³)
-1.91
Ti
0.52
H
-0.89
Ni

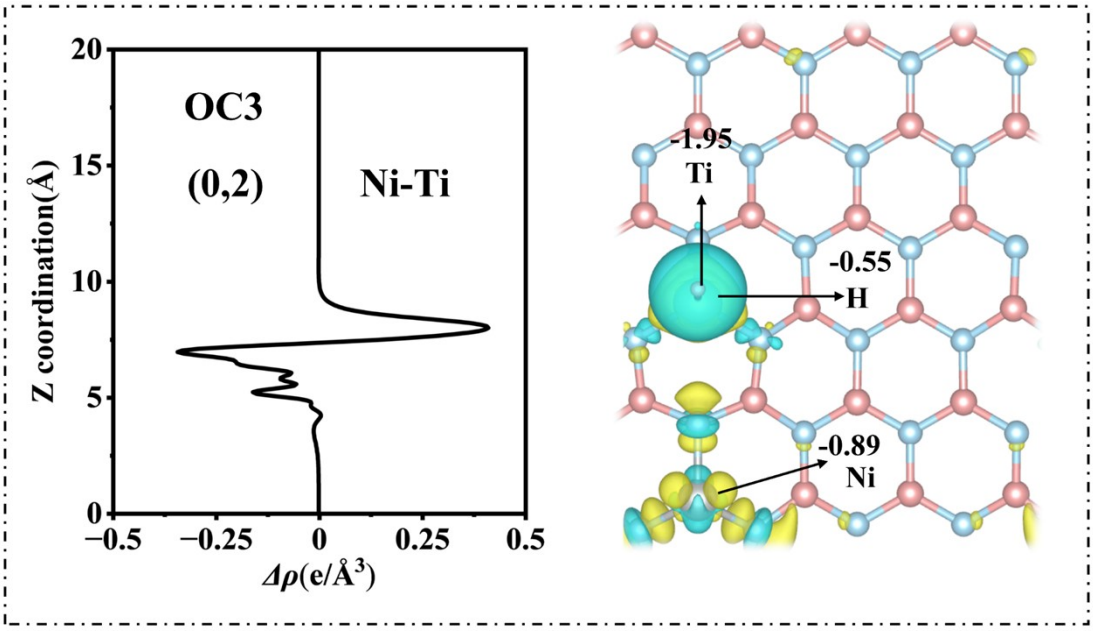


**Fig. S16** Differential charge density plots for randomly selected Ni- and Ti-doped structures at the OC1–OC3 sites.

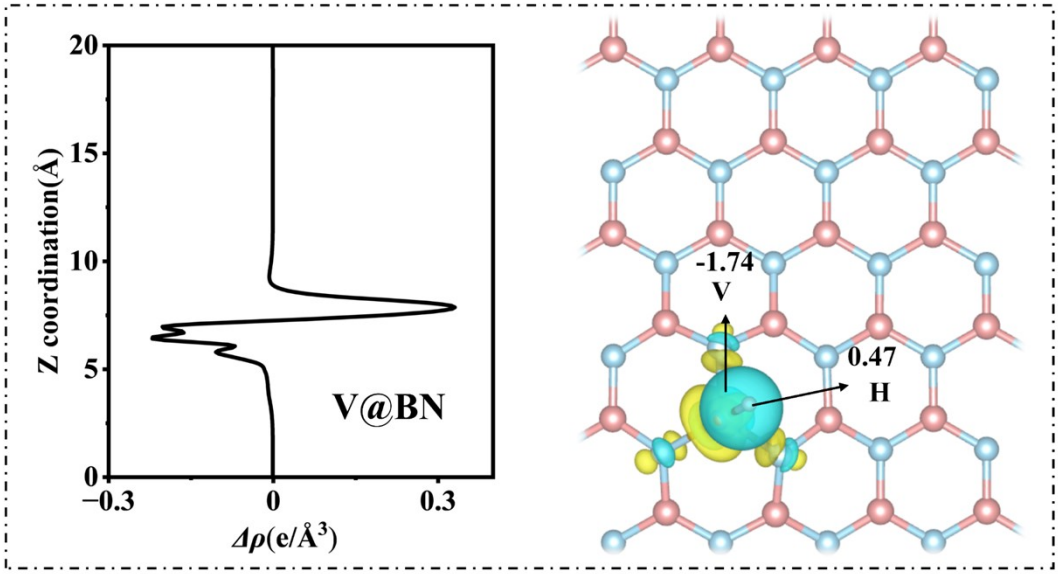
20
15
10
5
0
Z coordination(Å)
−0.3
0
0.3
Δρ(e/Å³)
V@BN
-1.74
V
0.47
H

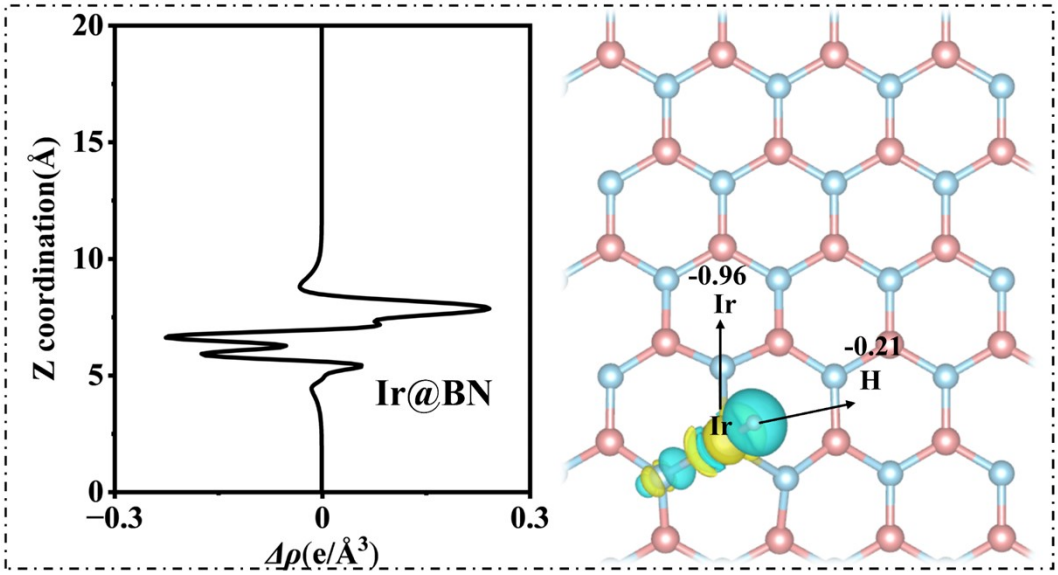
20
15
10
5
0
Z coordination(Å)
−0.3
0
0.3
Δρ(e/Å³)
Ir@BN
-0.96
Ir
-0.21
H
Ir

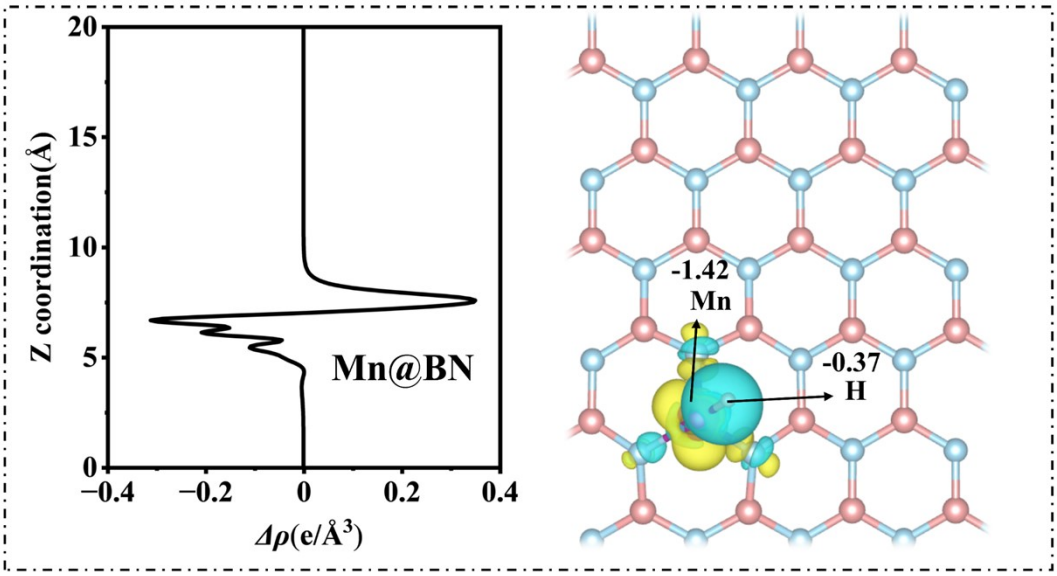
Z coordination(Å)
20
15
10
5
0
−0.4
−0.2
0
0.2
0.4
Δρ(e/Å³)
Mn@BN
-1.42
Mn
-0.37
H

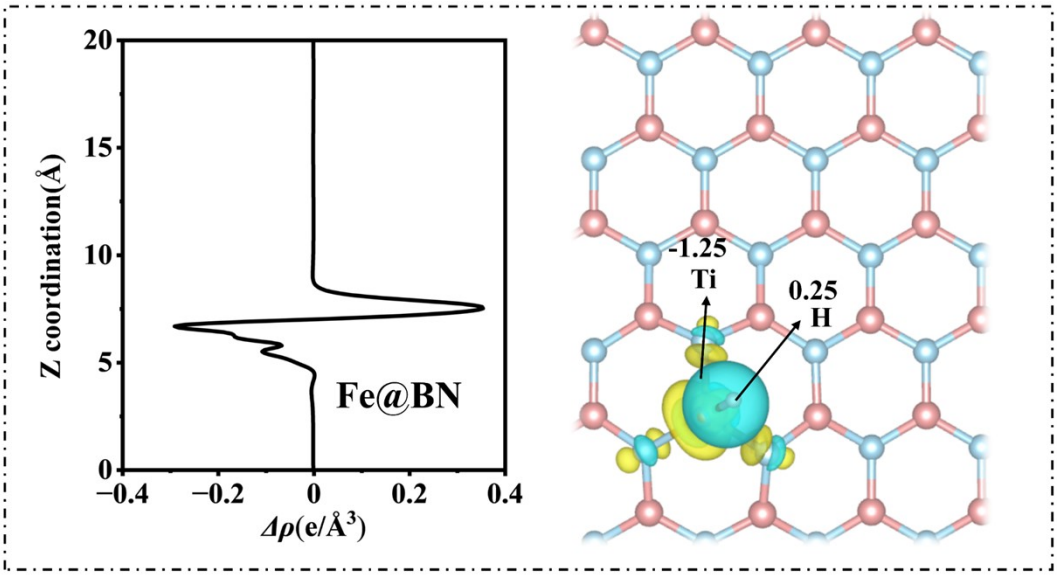
Z coordination(Å)
20
15
10
5
0
−0.4
−0.2
0
0.2
0.4
Δρ(e/Å³)
Fe@BN
-1.25
Ti
0.25
H

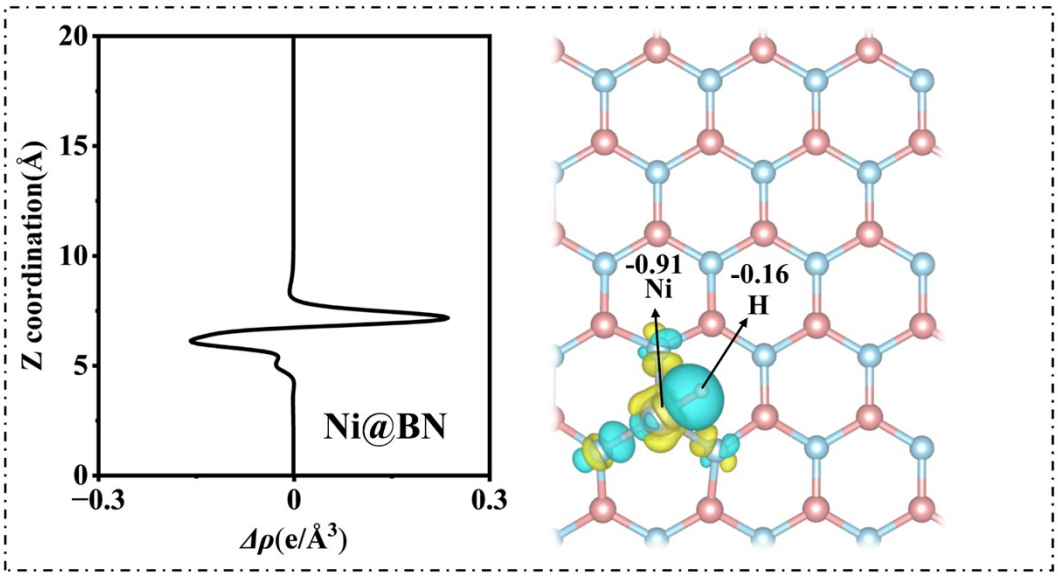
20
15
10
5
0
Z coordination(Å)
Ni@BN
−0.3
0
0.3
Δρ(e/Å³)
-0.91
Ni
-0.16
H

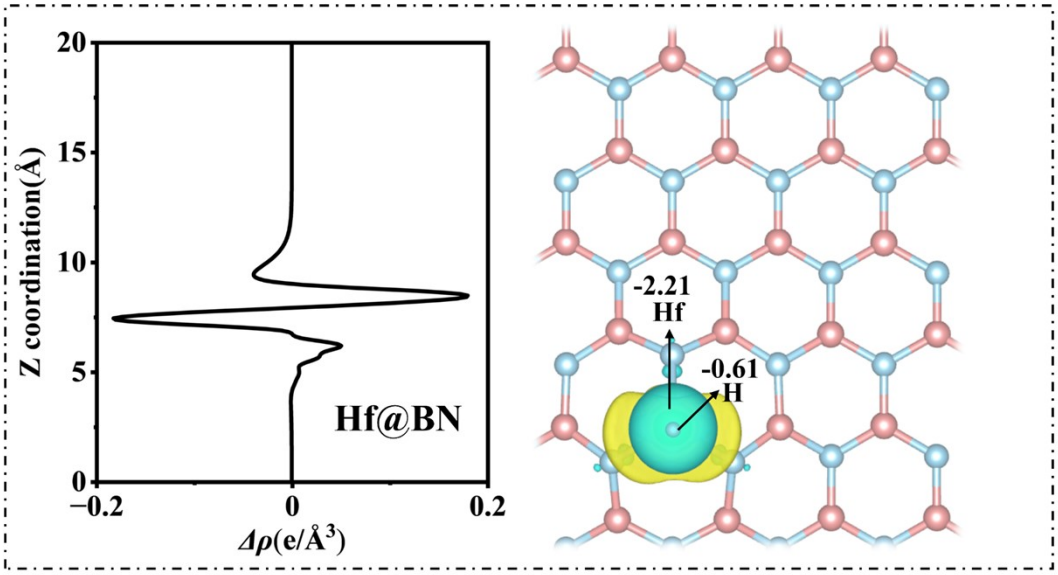
20
15
10
5
0
Z coordination(Å)
Hf@BN
−0.2
0
0.2
Δρ(e/Å³)
-2.21
Hf
-0.61
H

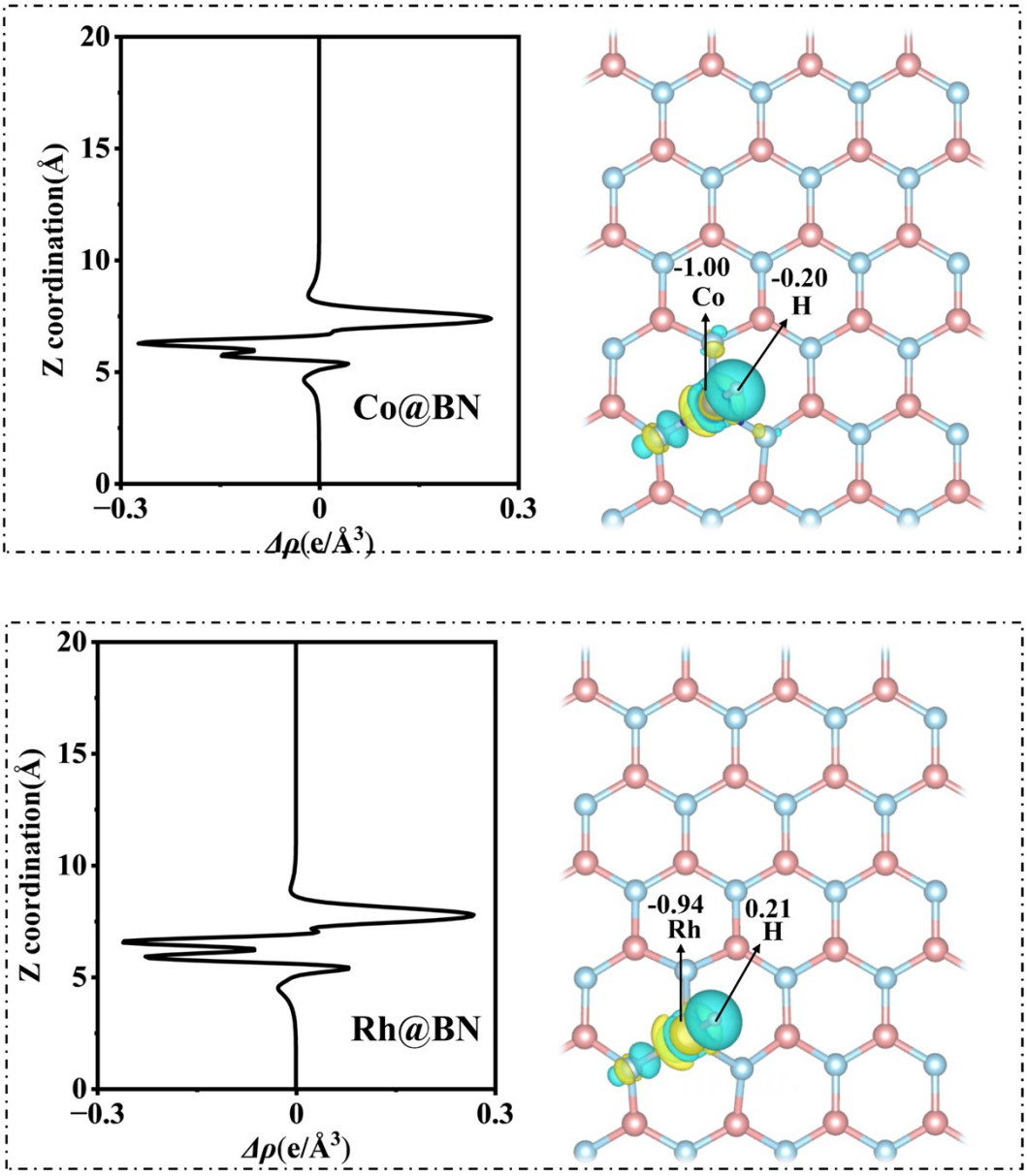


**Fig. S17** Differential charge density plots for randomly selected single-metal-doped BN structures.

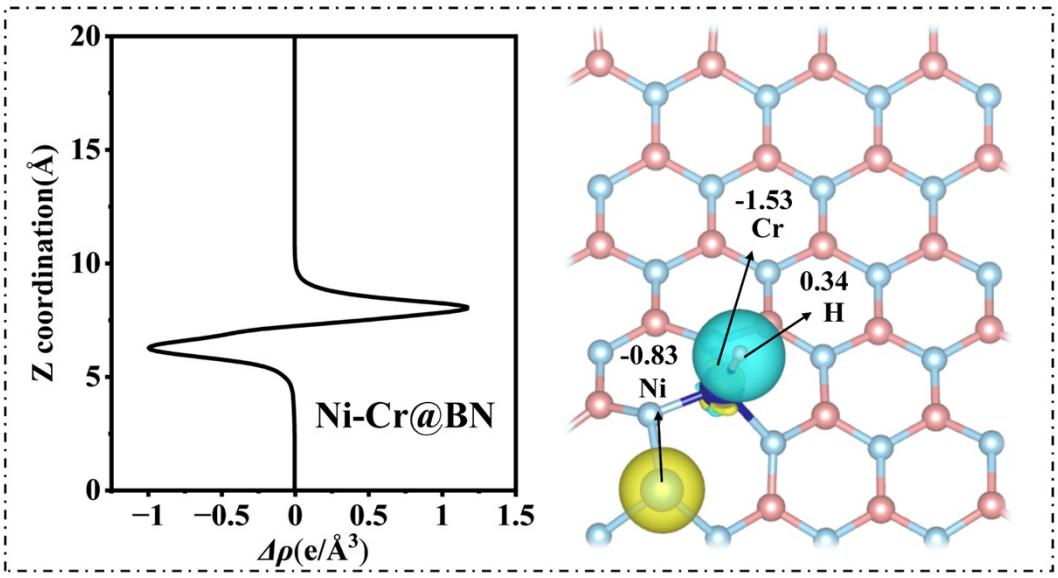
Z coordination(Å)
20
15
10
5
0
−1
−0.5
0
0.5
1
1.5
Δρ(e/Å3)
Ni-Cr@BN
-1.53
Cr
0.34
H
-0.83
Ni

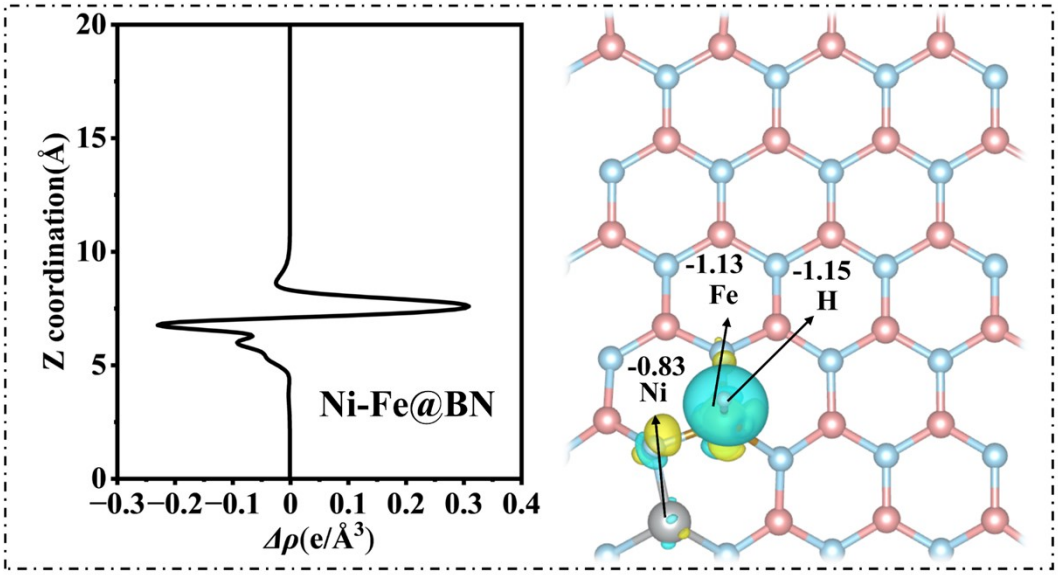
Z coordination(Å)
20
15
10
5
0
−0.3
−0.2
−0.1
0
0.1
0.2
0.3
0.4
Δρ(e/Å3)
Ni-Fe@BN
-1.13
Fe
-1.15
H
-0.83
Ni

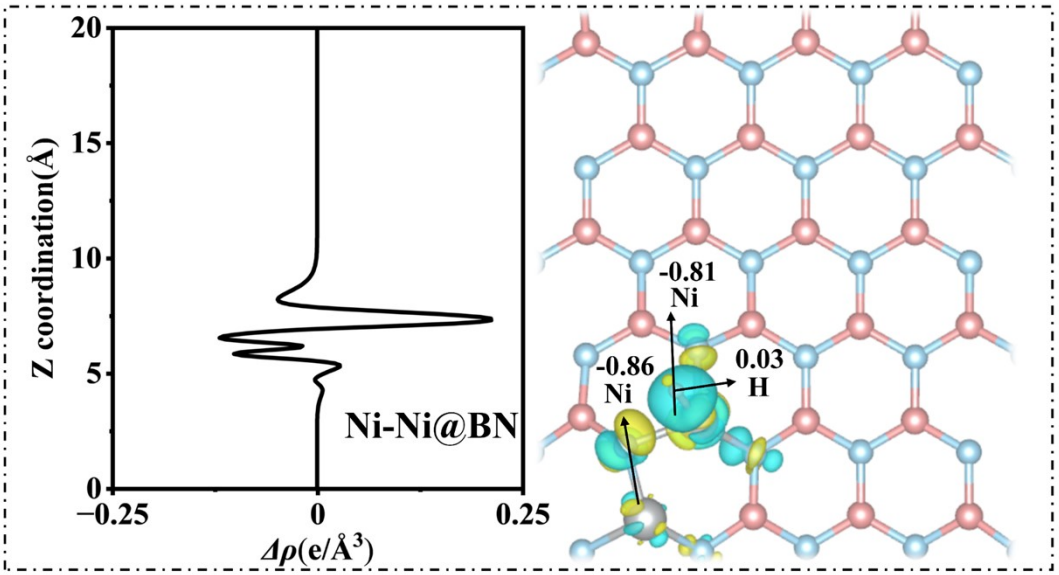
Z coordination(Å)
20
15
10
5
0
−0.25
0
0.25
Δρ(e/Å3)
Ni-Ni@BN
-0.81
Ni
-0.86
Ni
0.03
H

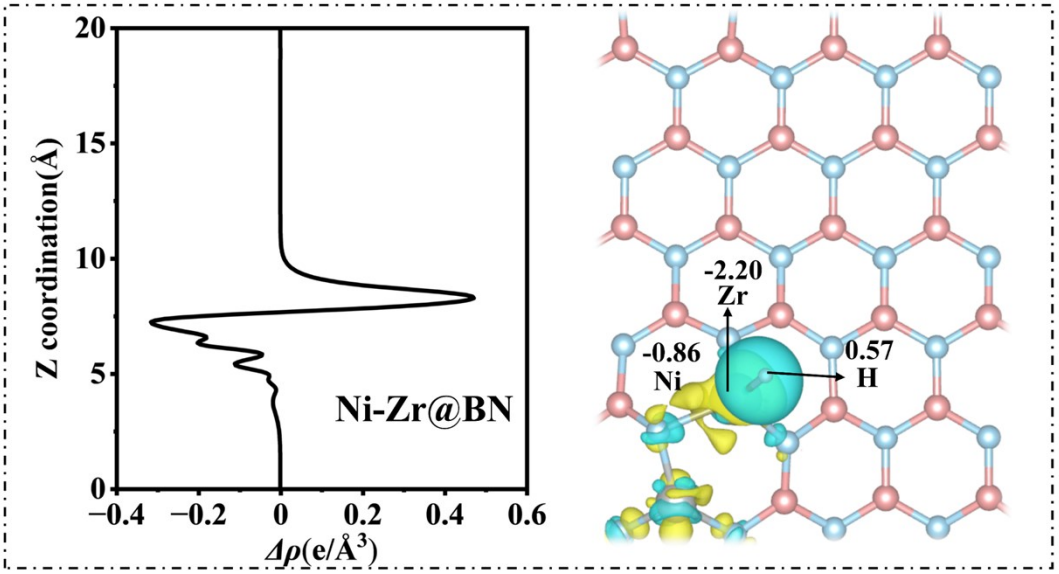
Z coordination(Å)
20
15
10
5
0
−0.4
−0.2
0
0.2
0.4
0.6
Δρ(e/Å3)
Ni-Zr@BN
-2.20
Zr
-0.86
Ni
0.57
H

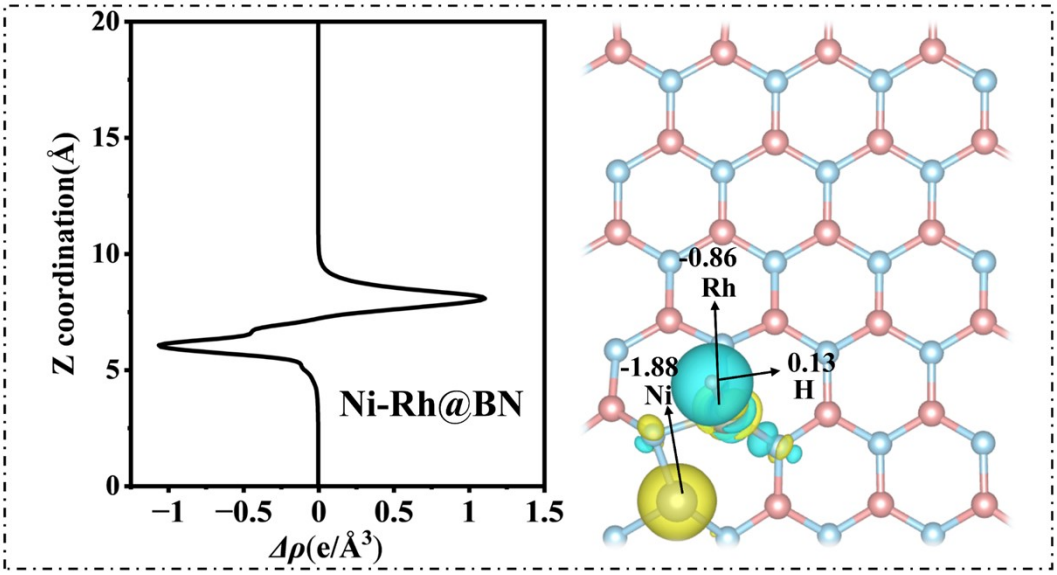
Z coordination(Å)
Δρ(e/Å³)
Ni-Rh@BN
-0.86
Rh
-1.88
Ni
0.13
H

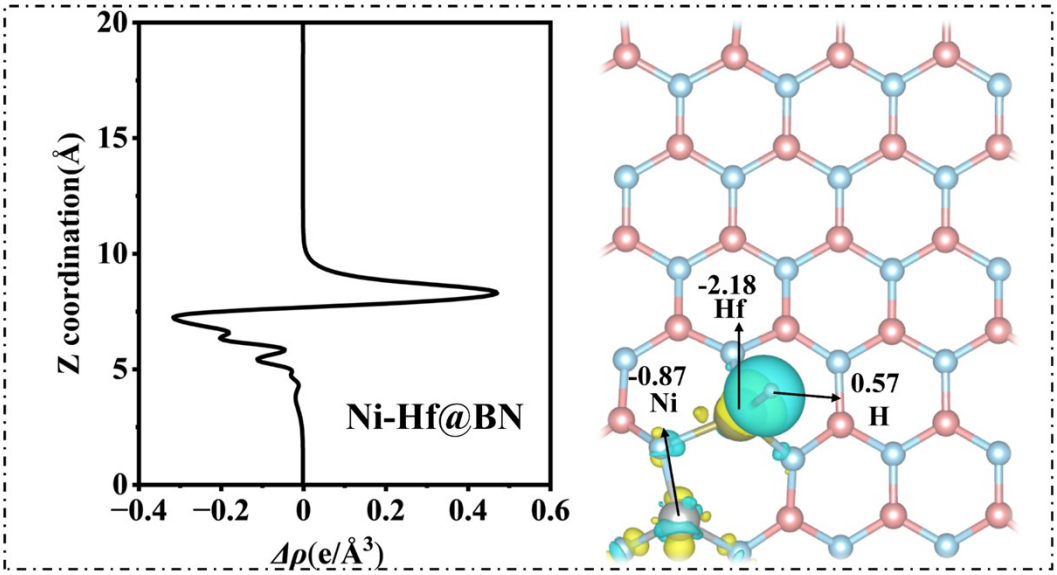
Z coordination(Å)
Δρ(e/Å³)
Ni-Hf@BN
-2.18
Hf
-0.87
Ni
0.57
H

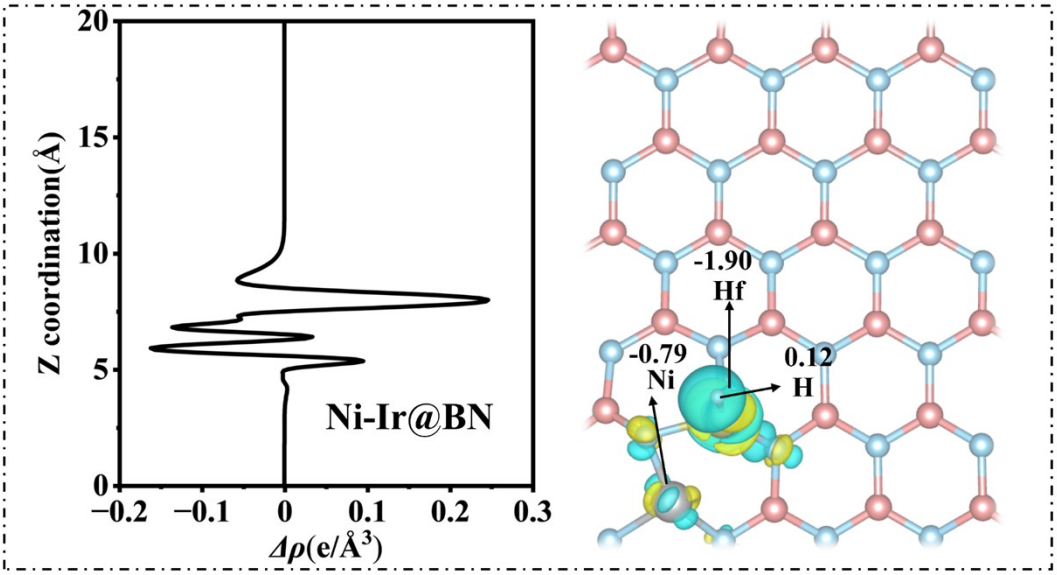


**Fig. S18** Differential charge density plots for randomly selected bimetal-doped BN structures.

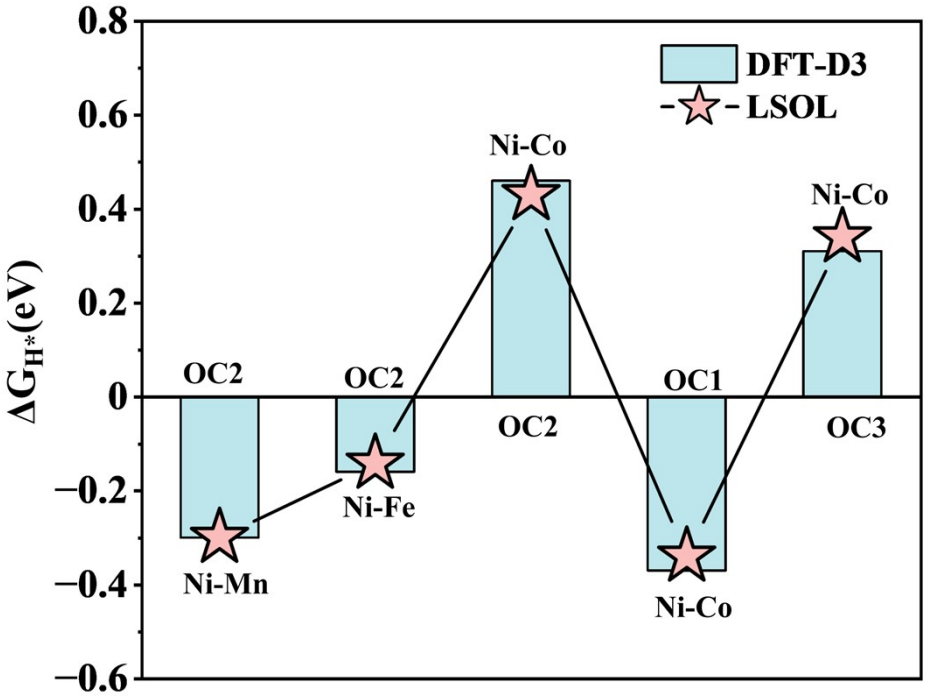


**Fig. S19** Comparison of HER calculation results under solvation conditions with those in vacuum.

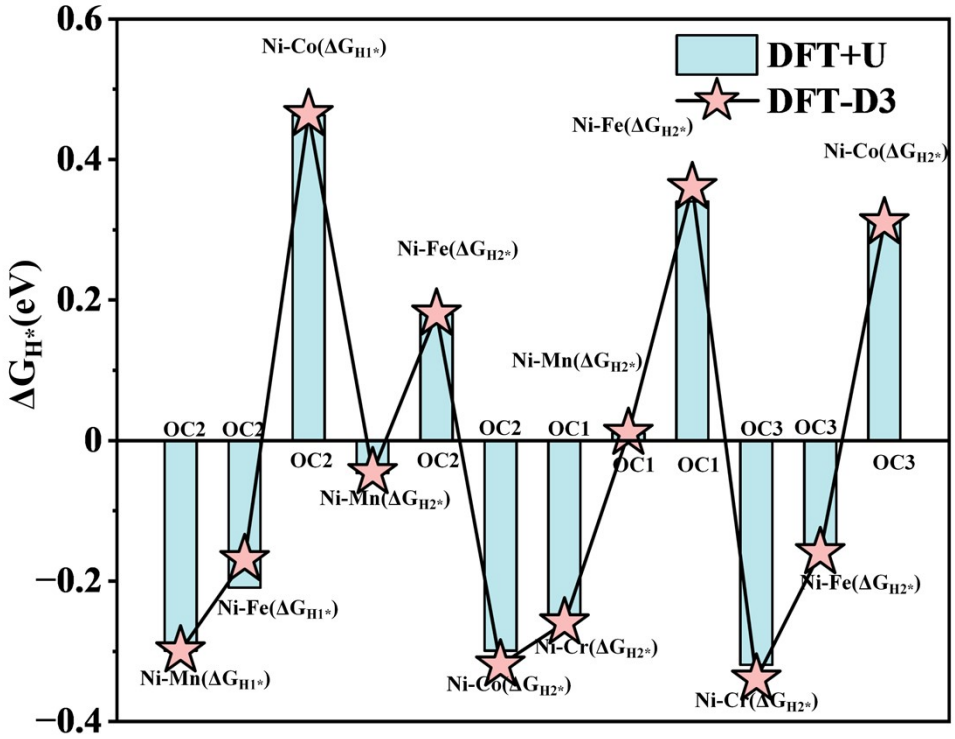


**Fig. S20** Comparison of HER calculation results under DFT+U conditions with those in vacuum.

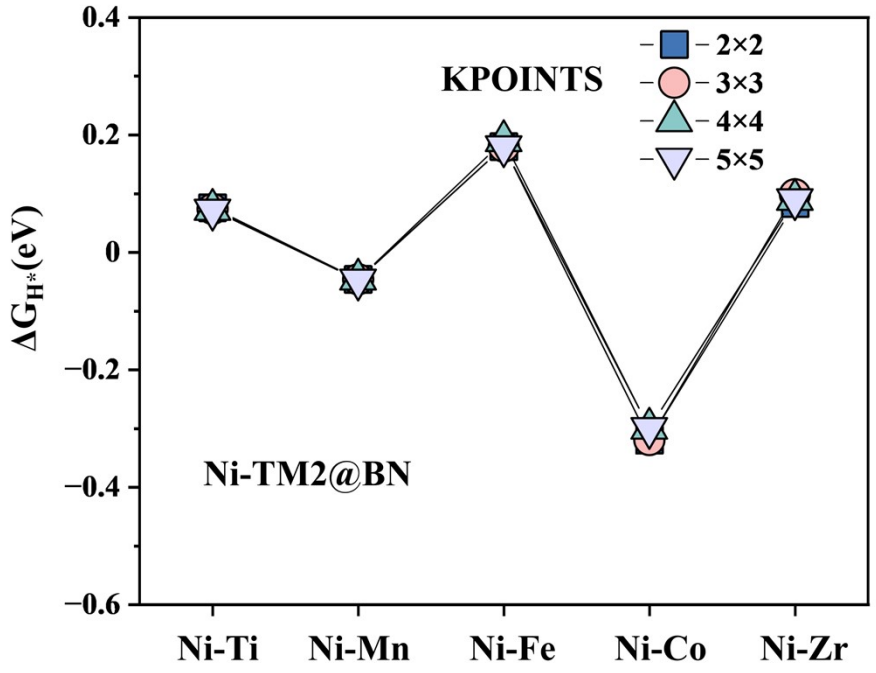


**Fig. S21** Effect of Different k-Point Meshes on the Gibbs Free Energy of Hydrogen Adsorption ($\Delta G_{H1*}$) for the Ni-TM2@BN System.

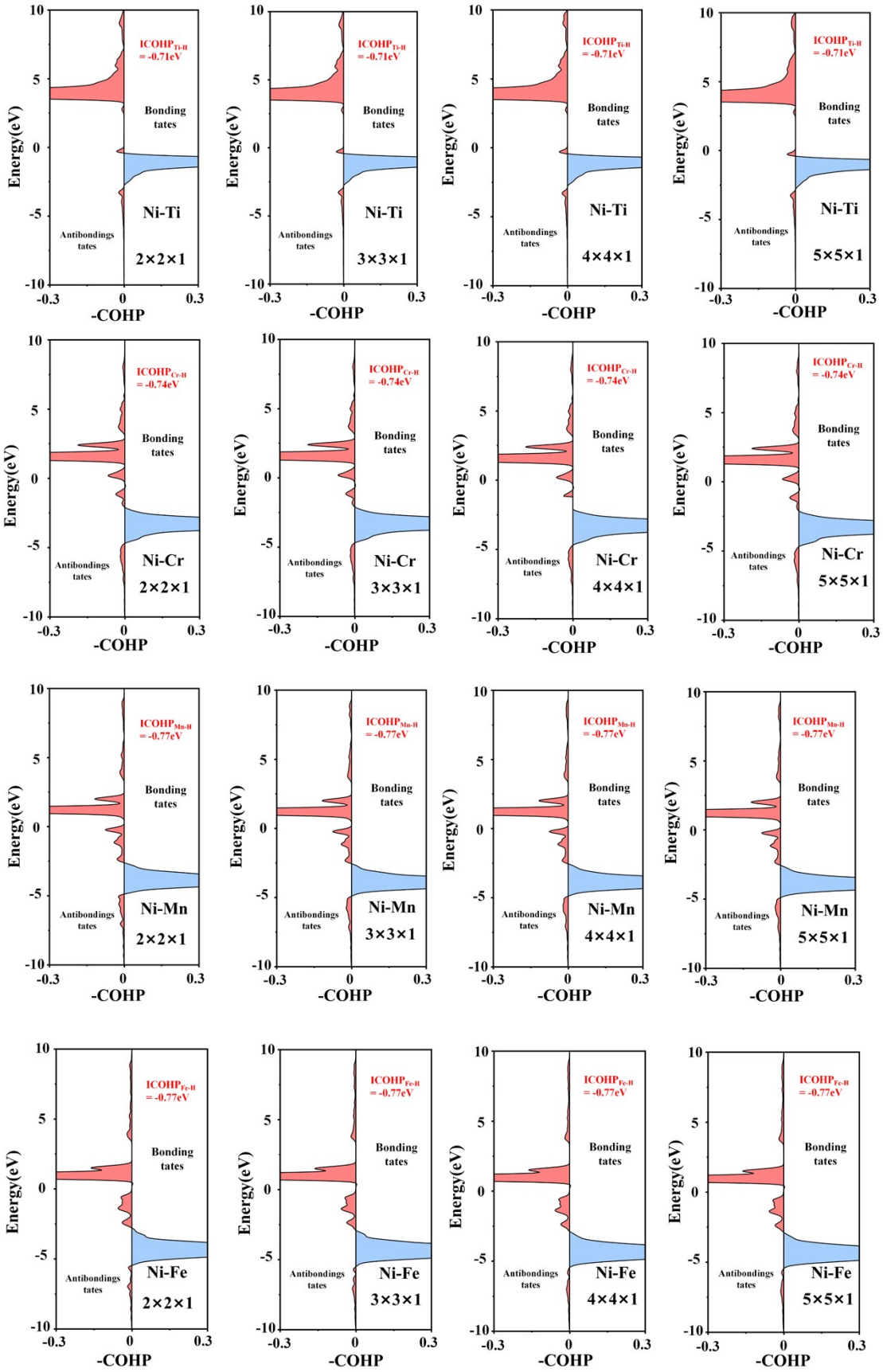


**Fig. S22** Crystal orbital Hamilton population (COHP) analysis for H intermediate adsorption on Ni–Ti, Ni–Cr, Ni–Mn, and Ni–Fe structures under different Monkhorst–Pack k-point samplings.

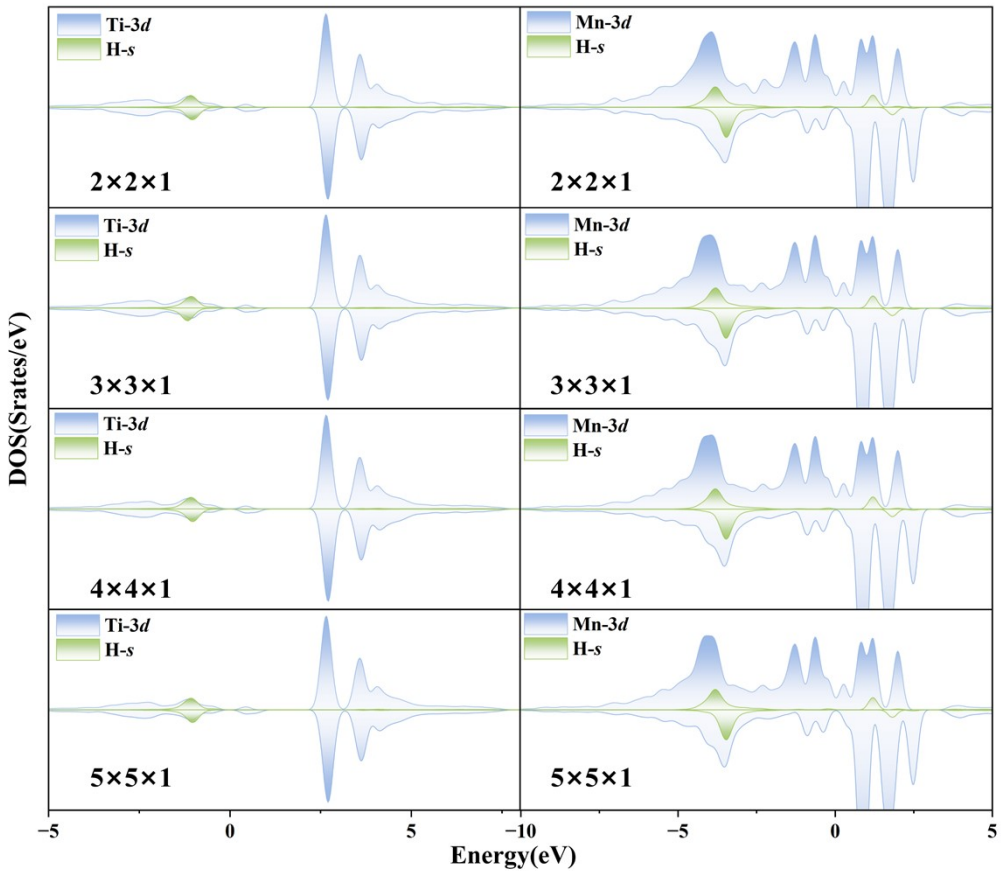
Ti-3d
H-s
2×2×1
Mn-3d
H-s
2×2×1
Ti-3d
H-s
3×3×1
Mn-3d
H-s
3×3×1
Ti-3d
H-s
4×4×1
Mn-3d
H-s
4×4×1
Ti-3d
H-s
5×5×1
Mn-3d
H-s
5×5×1
DOS(Srates/eV)
−5
0
5
−10
−5
0
5
Energy(eV)

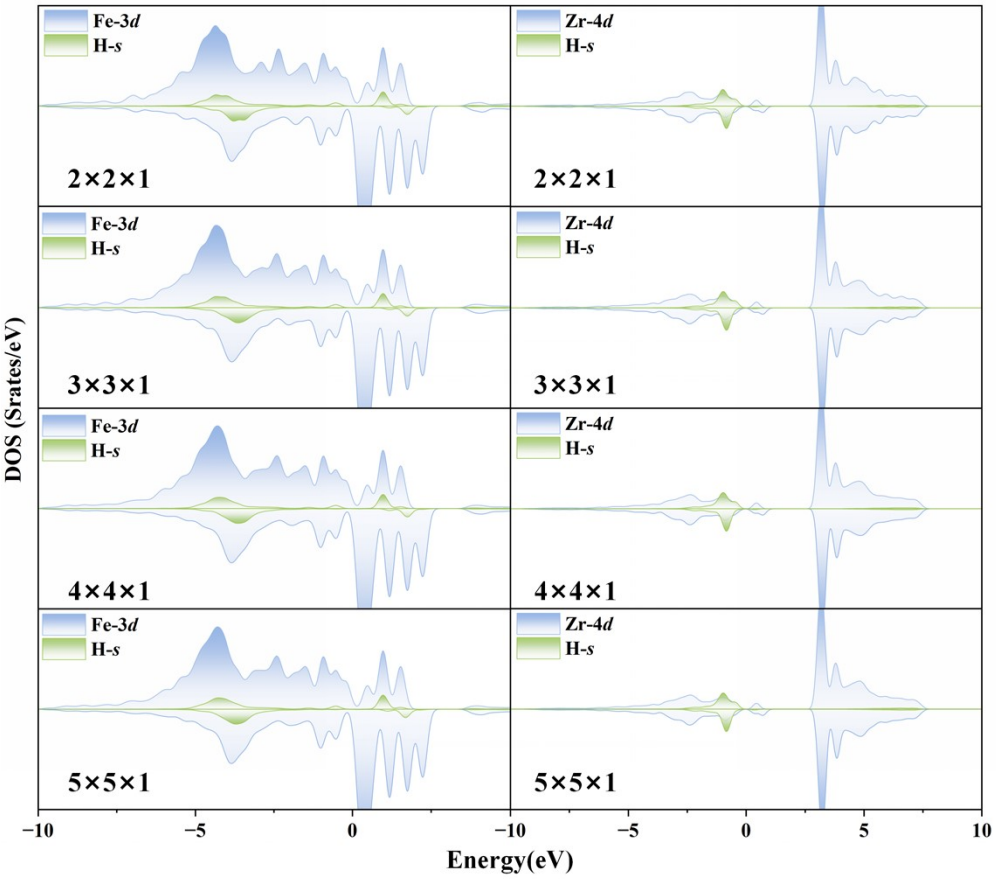
Fe-3d
H-s
2×2×1
Zr-4d
H-s
2×2×1
Fe-3d
H-s
3×3×1
Zr-4d
H-s
3×3×1
Fe-3d
H-s
4×4×1
Zr-4d
H-s
4×4×1
Fe-3d
H-s
5×5×1
Zr-4d
H-s
5×5×1
DOS (Srates/eV)
−10
−5
0
−10
−5
0
5
10
Energy(eV)

**Fig. S23** Density of states (DOS) of Ni–Ti, Ni–Mn, Ni–Fe and Ni–Zr structures under different Monkhorst–Pack k-point samplings.

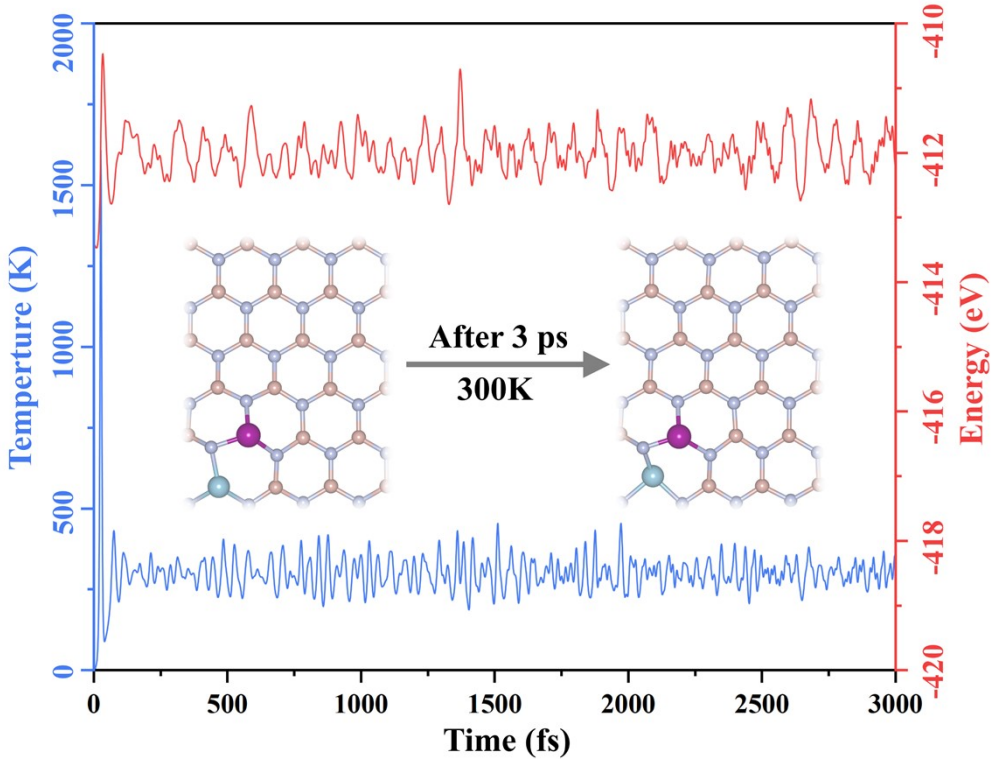


**Fig. S24** Temperature and energy evolution curves of the Ni-Mn@BN structure during ab initio molecular dynamics (AIMD) simulation at 300 K.

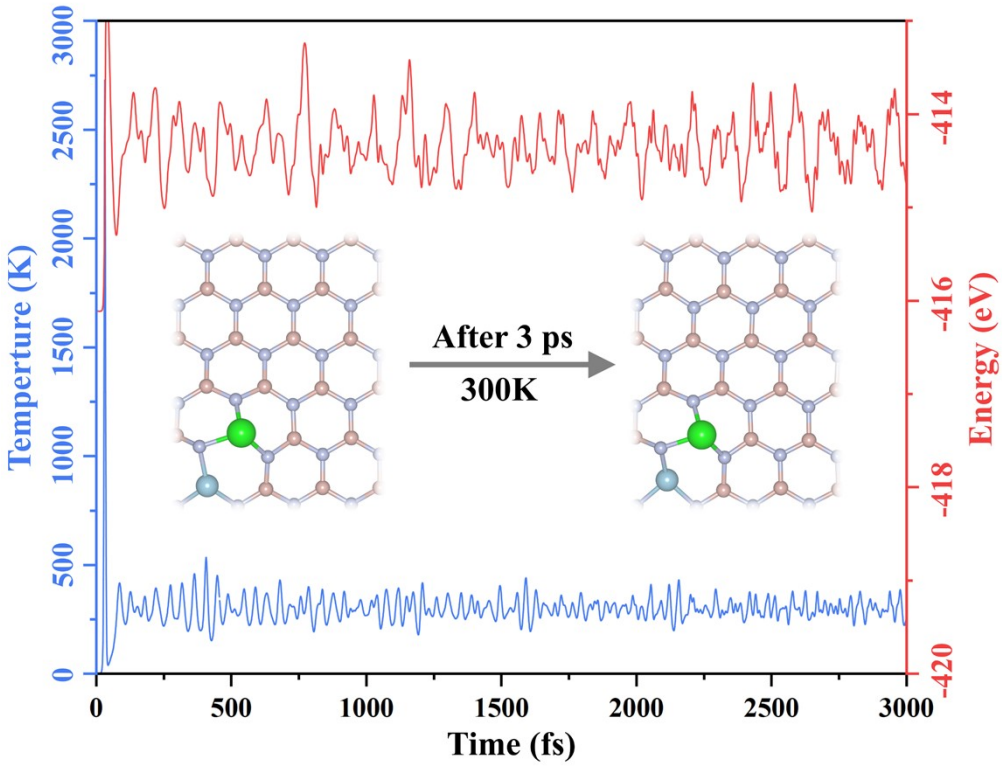


**Fig. S25** Temperature and energy evolution curves of the Ni-Zr@BN structure during ab initio molecular dynamics (AIMD) simulation at 300 K.

**References**

(1) G. Kresse, J. Furthmüller. Efficient iterative schemes for ab initio total-energy calculations using a plane-wave basis set. *Physical Review B*. 1996, *54*(16), 11169-11186.

(2) B.o. Dec, R. Bogdanowicz, K. Pyrchla. Ab-initio study of electrical and optical properties of allylamine. *Photonics Letters of Poland*. 2018, *10*(3), 94-96.

(3) S. Grimme. Semiempirical GGA-type density functional constructed with a long-range dispersion correction. *Journal of Computational Chemistry*. 2006, *27*(15), 1787-1799.

(4) M. Sipper, J.H. Moore. Conservation machine learning. *BioData Mining*. 2020, *13*(1), 9.

(5) X. Jia, H. Li. Machine learning enabled exploration of multicomponent metal oxides for catalyzing oxygen reduction in alkaline media. *Journal of Materials Chemistry A*. 2024, *12*(21), 12487-12500.

(6) N.K.B. Christoph Höner zu Siederdissen , Markus Cornberg. Reply to Liaw. *The Journal of Infectious Diseases*. 2018, *218*(11), 1853-1854.

(7) K. Fereydooni, O. Nordness. Predicting the Properties of IL-Solvent Electrolytes Using a Hybrid Support Vector Classification and Gradient Boosting Regression (SVC-GBR) Framework. *Industrial & Engineering Chemistry Research*. 2025, *64*(39), 19281-19294.

(8) Y. Xu, Q. Qian. i-SISSO: Mutual information-based improved sure independent screening and sparsifying operator algorithm. *Engineering Applications of Artificial Intelligence*. 2022, *116* 105442.